

EFFECT OF INORGANIC PARTICLES IN THE PROTECTION BEHAVIOR  
OF EPOXY-BASED COMPOSITE COATINGS

A Dissertation

by

BRENDA CAROLINA GALICIA AMARO

Submitted to the Graduate and Professional School of  
Texas A&M University  
in partial fulfillment of the requirements for the degree of

DOCTOR OF PHILOSOPHY

Chair of Committee,	Homero Castaneda-Lopez
Co-Chair of Committee,	Raymundo Case
Committee Members,	Hong Liang
	Kelvin Xie
Head of Department,	Ibrahim Karaman

August 2021

Major Subject: Materials Science and Engineering

Copyright 2021 Brenda Carolina Galicia Amaro

## ABSTRACT

This research focuses on understanding the different mechanisms underlying the performance of two epoxy-based coatings applied on different substrates.

The magnesium-rich coatings applied to aluminum 7075 T6 work aims to use electrochemical methods, such as open circuit potential and electrochemical impedance spectroscopy (EIS) to characterize the real-time performance of a magnesium-rich epoxy coating primer (MgRP) varying in magnesium content and exposed to a neutral buffer solution. The magnesium-rich primer (MgRP) illustrates the evolution of the sacrificial and barrier effects with different amounts of Mg particles and carbon nanotubes (CNTs) added to the epoxy matrix. The results can be used to characterize the performance of this coating/substrate system under a neutral environment condition.

The epoxy-trimetallic oxide (Epoxy-TMO) coatings were synthesized and integrated on stainless steel surface in order to study the effect of the trimetallic oxides (TMO)  $ZrO_2/TiO_2/ZnO$  ( $Z^2T$ ) for the barrier properties of the epoxy polymer matrix. The different ratios of TMO were synthesized using the ball-milling method and later dispersed on the polymer matrix. Elemental characterization and morphological studies of the oxides were performed with x-ray diffraction (XRD) and SEM. The thickness of the epoxy-TMO coatings was estimated using SEM cross-sectional imaging. UV-Vis was performed to study the light absorption properties of the coatings. The effect of the addition of these oxides on the electrochemical behavior was studied in a 3.5 wt% NaCl solution using electrochemical impedance spectroscopy (EIS) and linear polarization resistance (LPR). The epoxy-TMO coating with a ratio of 50/40/10  $Z^2R$  hybrid showed the highest corrosion resistance and the formation of a second protective barrier following 28 days in the

corrosive environment. The proposed mechanisms consider the effect of the oxides in corrosion control actions and the natural barrier effect due to the polymer matrix. The results show that the combination of these three oxides in the polymer matrix increases the barrier properties.

## ACKNOWLEDGEMENTS

I would like to thank my committee chair, Dr. Castaneda, and my committee members, Dr. Case, Dr. Liang, and Prof. Xie, for their guidance and support throughout the course of this research.

Thanks also go to my friends and colleagues and the department faculty and staff for making my time at Texas A&M University a great experience.

Finally, thanks to my family for their encouragement, patience, and love.



## CONTRIBUTORS AND FUNDING SOURCES

### **Contributors**

This work was supported by a dissertation committee consisting of Dr. Castaneda [advisor], Dr. Case and Dr. Xie of the Department of Materials Science and Engineering and Dr. Liang of the Department of Mechanical Engineering at Texas A&M University.

The X-Ray Diffractogram (XRD) and UV-Vis Spectra Analysis tests were performed by Dr. Subramaniam and his group at Cinvestav-Zacatenco-LENE facilities.

All other work conducted for the dissertation was completed by the student independently.

### **Funding Sources**

Graduate study was supported by assistantship from Texas A&M University, an scholarship from CONACyT-Mexico, and financial support by Roberto Rocca Foundation.

## NOMENCLATURE

CNTs	Carbon nanotubes
PVC	Pigment volume concentration
TMO	Trimetallic oxide
CPVC	Critical pigment volume concentration
MgRP	Magnesium-rich epoxy primer
AA7075	Aluminum Alloy 7075
SS	Stainless Steel
Mg	Magnesium
NaCl	Sodium Chloride
SCE	Saturated calomel electrode
OCP	Open circuit potential
EIS	Electrochemical impedance spectroscopy
SEM	Scanning electron microscopy
EDS	Energy dispersive X-ray spectroscopy
XRD	X-ray diffraction
UV-Vis	Ultraviolet-visible spectroscopy
XPS	X-ray photoelectron spectroscopy
CPE	Constant phase element
$Y_0$	Admittance
$R_c$	Coating resistance
$C_{c,eff}$	Effective capacitance of the coating
$R_{ct}$	Charge transfer resistance

$C_{dl}$	Capacitance of the double layer
$W_s$	Warburg impedance
$L$	Inductance
$R_L$	Resistance of the adsorption process
$C_{ox}$	Capacitance of the layer of corrosion products
$R_{ox}$	Resistance of the layer of corrosion products

## TABLE OF CONTENTS

	Page
ABSTRACT.....	ii
ACKNOWLEDGEMENTS.....	iv
CONTRIBUTORS AND FUNDING SOURCES .....	v
NOMENCLATURE .....	vi
TABLE OF CONTENTS.....	viii
LIST OF FIGURES .....	x
LIST OF TABLES.....	xii
CHAPTER I INTRODUCTION AND LITERATURE REVIEW .....	1
I.1. Hypothesis .....	1
I.2. Epoxy resins for corrosion protection .....	2
I.3. Aluminum alloy 7075.....	3
I.3.1. Physical properties of aluminum alloy AA7075.....	4
I.3.2. Mechanical properties of aluminum alloy AA7075.....	5
I.3.3. Primary applications of aluminum alloy AA7075 .....	7
I.3.4. Corrosion of aluminum alloys .....	7
I.3.5. Coating technologies for prevention and control of corrosion of aluminum alloys.....	10
I.4. Mg-rich epoxy coatings.....	11
I.4.1. Use of Mg alloys instead of pure Mg particles .....	13
I.4.2. Additional corrosion inhibitive components to improve Mg-rich performance... ..	14
I.4.3. Multifunctional and hybrid coatings with carbon nanotubes (CNTs) .....	16
I.4.4. Factors influencing the behavior of Mg-rich epoxy primers (MgRPs).....	17
I.4.5. Techniques for performance evaluation of Mg-rich epoxy coatings .....	18
I.4.6. Electrochemical impedance spectroscopy to study the electrochemical behavior of Mg-rich epoxy primer.....	18
I.5. Stainless steel.....	20
I.5.1. Types of stainless steels .....	20
I.5.2. Coatings design for stainless steel .....	23

	Page
CHAPTER II ELECTROCHEMICAL INVESTIGATION OF THE SYNERGIC EFFECT BETWEEN MAGNESIUM PARTICLES AND CARBON NANOTUBES IN EPOXY COATING .....	24
II.1. Introduction .....	24
II.2. Experimental procedure .....	26
II.2.1. Electrolyte solution .....	26
II.2.2. Coated samples .....	27
II.2.3. Electrochemical measurements.....	28
II.2.4. Materials characterization.....	29
II.3. Results and analysis .....	30
II.3.1. Open Circuit Potential (OCP).....	30
II.3.2. Mg content influence on the evolution of corrosion control performance .....	33
II.3.2.1. MgR 15%.....	33
II.3.2.2. MgR 30%.....	36
II.3.2.3. MgR 60%.....	38
II.3.3. Influence of CNTs on the evolution and interfacial mechanisms.....	40
CHAPTER III NANOCOMPOSITE EPOXY-RICH COATINGS.....	46
III.1. Introduction.....	46
III.2. Experimentation.....	47
III.2.1. Materials .....	47
III.2.2. Synthesis of the trimetallic oxide compounds .....	47
III.2.3. Preparation and deposition of the epoxy-TMO coatings .....	48
III.2.4. Characterization .....	48
III.3. Results and discussion .....	50
III.3.1. X-ray Diffractogram analysis .....	50
III.3.2. Morphological characterization of trimetallic oxides .....	51
III.3.3. Raman analysis .....	53
III.3.4. Optical analysis of epoxy-rich coating .....	53
III.3.5. Contact Angle measurements .....	56
III.3.6. Electrochemical Characterization .....	57
CHAPTER IV CONCLUSIONS.....	70
IV.1. Magnesium-rich coating .....	70
IV.2. Trimetallic oxides .....	70
REFERENCES .....	71

## LIST OF FIGURES

FIGURE		Page
1	The electrochemical series versus the standard calomel electrode (SCE).....	12
2	Schematic representation of metal-rich primers onto an aluminum substrate.....	13
3	Z  modulus at 0.01Hz vs. PVC for Mg-rich epoxy/polyamide primers at pH = 6.2 in 3% NaCl Location of Study Area .....	19
4	General chemical composition of stainless steel .....	21
5	Schematic distinction between steel and stainless steel.....	21
6	Experimental set up.....	29
7	OCP evolution for different Mg and CNT concentrations exposed to buffer solution at pH=7.....	31
8	EIS Nyquist and Bode plots for Mg-rich primer-aluminum system without CNTs.	35
9	Proposed mechanism of protection conferred by the 15% Mg coating.....	37
10	EIS Nyquist and Bode plots for Mg-rich primer-aluminum system with carbon nanotubes .....	41
11	SEM and EDS of 15% Mg and 30% Mg coatings before immersion .....	44
12	SEM and EDS of a) 30% Mg 0% CNT and b) 30% Mg 0.77% CNT coatings after immersion .....	44
13	Equivalent circuit.....	45
14	XRD of the synthesized TMO ZrO <sub>2</sub> : ZnO: TiO <sub>2</sub> by ball milling .....	50
15	A) SEM micrographs of TMO (ZrO <sub>2</sub> /ZnO/TiO <sub>2</sub> ), B) Cross-section SEM images of epoxy-TMO coating in a stainless steel substrate.....	52
16	Raman of the epoxy- TMO coatings at different ratios of ZrO <sub>2</sub> / TiO <sub>2</sub> / ZnO: Epoxy-A (90/5/5), Epoxy-B (80/10/10), Epoxy-C (65/25/10), Epoxy-D (50/40/10), Epoxy-E (40/50/10) .....	54

17	UV absorbance of the synthesized epoxy- TMO coatings: Epoxy-A (90/5/5), Epoxy-B (80/10/10), Epoxy-C (65/25/10), Epoxy-D (50/40/10), Epoxy E (40/50/10).....	55
18	Nyquist (a), Bode (b) and phase angle (c) of the epoxy and epoxy-TMO coatings at Day 21 .....	61
19	Nyquist and phase diagrams of the stainless steel (a-b), and the scratched coatings epoxy (c-d) and epoxy-TMO coatings at different ratios of ZrO <sub>2</sub> /TiO <sub>2</sub> /ZnO: Epoxy-A (90/5/5) (e-f), Epoxy-B (80/10/10) (g-h), Epoxy-C (65/25/10) (i-j), Epoxy-D (50/40/10) (k-l), Epoxy-E (40/50/10) ) (m-n).....	62
20	Bode (a), phase angle (b), Nyquist (c) and equivalent circuit (d) of the epoxy and epoxy-TMO scratched coatings at Day 21.....	66
21	Corrosion protection mechanism of the epoxy coatings, a) physical interaction of the nanoparticles with the epoxy polymer, b) day 1, c) day 7, d) day 14, e) day 21, f) day 28 .....	69

## LIST OF TABLES

TABLE		Page
1	Chemical composition of aluminum alloy 7075 (%wt.).....	5
2	Mechanical properties of aluminum alloy (AA7075).....	6
3	Galvanic series .....	9
4	Chronology Mg-rich primers .....	15
5	Values of equivalent circuit fitting.....	45
6	Composition of trimetallic oxides (wt%).....	48
7	Average crystallize size of the TMO oxides.....	51
8	Elemental compositional for cross-section image of epoxy film with different trimetallic oxide compositions.....	52
9	Contact angle measurements of epoxy-TMO coatings.....	58
10	EIS fitting analysis of the scratched epoxy and epoxy-TMO coatings.....	66
11	Linear polarization resistance (LPR) of the coatings at 21 days .....	69



CHAPTER I  
INTRODUCTION AND LITERATURE REVIEW

**I.1. Hypothesis**

The performance of an epoxy-rich coating can be modified and improved through the addition of particles.

Depending on the composition, concentration, and size of the particles, an epoxy-rich coating can have different functions, such as cathodic protection, enhanced barrier performance, self-healing, or self-cleaning abilities.

The proposed research should be able to address the following questions:

- How does the content of magnesium affect the cathodic protection performance of a coating?
- How do the content and distribution of magnesium influence the barrier and cathodic protection behavior of a coating?
- Does the addition of carbon nanotubes improve the barrier and cathodic protection functionality of a coating?
- Can the barrier performance of a coating be increased through the addition of smaller particles?
- Does the addition of zirconium oxide, zinc oxide, and titanium oxide confer self-healing and self-cleaning abilities to coatings?

## **I.2. Epoxy resins for corrosion protection**

Owing to their high adhesive properties and low cost, epoxy resins have been extensively used for structural adhesive applications in the aerospace industry. Epoxy resins reinforced with high-strength glass, carbon, Kevlar, or boron fibers have the greatest potential for use in the aerospace industry [1, 2].

Epoxy resins are thermosetting resins, which are cured with a wide variety of curing agents via curing reactions. Their properties depend on the specific combination of epoxy resins and curing agents used [3-5]. Because of their excellent mechanical properties and good heat and chemical resistance, epoxy resins are currently used across a wide range of fields, where they serve as fiber-reinforced materials, general-purpose adhesives, high-performance coatings, and encapsulating materials [6].

The highly cross-linked epoxy resins are rigid and brittle and have relatively poor resistance to crack initiation and growth, thus limiting their use in many applications, such as structural materials. Many efforts have aimed to improve their physical properties by using various toughening or strengthening agents.

Several inorganic particles have been added to epoxy resins to improve or change their properties. The incorporation of inorganic particles modifies the protective mechanism of the structure against corrosion. This type of coating is typically called a composite epoxy-based coating.

Epoxy resins commonly provide a physical barrier between the substrate and the electrolyte. The addition of inorganic particles confers another type of protection called sacrificial protection, which is achieved when a more reactive material is in contact with the

substrate. For example, pieces of zinc alloy are attached to pump bodies and pipes, and the protected metal becomes the cathode and does not corrode.

This research focuses on understanding the reaction mechanism of two types of composite epoxy-based coatings applied on different substrates. The first system is a magnesium-rich primer, provided by Tesla Nanocoatings, which was spread on aluminum. The second system was developed in our laboratory by adding functional nanoparticles (Ti, Zn, and Zr) and was applied on stainless steel.

Magnesium-rich primers are designed to provide a barrier and cathodic protection for the substrate. In contrast, nanocomposite coatings are intended to mitigate the effects of macro-sized particles in the durability of a coating by reducing the pore size of the polymeric phase.

### **I.3. Aluminum alloy 7075**

Aluminum and its alloys are widely used in transportation, including marine, automotive, and aviation applications, because of their high strength-to-density ratio. Their excellent mechanical properties, including low density, and good thermal and electrical conductivity, make aluminum and its alloys promising in several key engineering applications. Chemical resistance is an important property for engineering structures in harsh and extreme environments [7-9].

Aluminum, generally has good resistance to corrosion, owing to the formation of an oxide layer film that is strongly bonded to its surface. The main alloying elements used with aluminum are magnesium, silicon, manganese, copper, and zinc. However, during pre-processing and casting, aluminum and its alloys gain or increase the number of impurities. Despite having an optimal

strength to weight ratio, aluminum alloys are highly susceptible to localized attack [10], such as pitting, and intergranular corrosion.

Aluminum alloys are considered strong, light metals with many important industrial applications. Alloys are mixtures of metals with greater utility than their constituents. Specific properties of pure aluminum are improved by the presence of small quantities of different metals, known as alloying elements. Alloys have been developed to provide stronger, more conductive, and/or more resilient materials for designing new applications, and they have revolutionized engineering capabilities. Aluminum is a common metal with many valuable alloys. The Aluminum Association has defined a classification method for some of these alloys by using a numbered-naming system comprising the alloying elements. The present work is focused on the 7xxx series of alloys that use zinc as their main alloying element, specifically the 7075 aluminum alloy. Three additional digits refer to individual alloys in the series. In engineering applications, 7075 aluminum alloy is one of the most relevant alloys, and it has been used extensively in aircraft structures because of its high strength-to-density ratio, among other characteristics [11].

### **I.3.1. Physical properties of aluminum alloy AA7075**

The aluminum alloy AA7075 has zinc as its primary alloying element; its chemical composition is shown in **Table 1**. It has a density is  $2.81 \text{ g/cm}^3$  ( $0.102 \text{ lb/in}^3$ ). The 7075 aluminum alloy is considered one of the strongest aluminum alloys, and it is considered valuable in high-stress applications. The content of copper in 7075 aluminum confers susceptibility to corrosion; however, its presence is necessary to obtain better and stronger material.

### I.3.2. Mechanical properties of aluminum alloy AA7075

The mechanical properties of the 7075 Aluminum alloy can be improved through strengthening with a heat treatment known as “tempering.” The process requires high temperature (300-500 °C) to reconfigure the crystalline structure of the metal to increase its toughness. T6 tempered 7075 aluminum alloy is a temper for aluminum plate and bar stock. Importantly, each tempering process gives 7075 aluminum its distinct characteristics.

**Table 1.** Chemical composition of aluminum alloy 7075 (%wt.) [12]

Element	% Composition
Copper	1.2 – 2.0
Magnesium	2.1–2.9
Zinc	5.1–6.1
Chromium	0.18–0.28
Silicon	0–0.40
Titanium	0–0.2
Aluminum	Balance

This alloy has significant mechanical properties and possesses superior ductility, high strength, and excellent resistance to fatigue. It is more prone to fragilization by embrittlement than other aluminum alloys owing to micro-segregation; however, it has considerable better corrosion resistance than the alloys from other series.

The elasticity modulus of 7075 aluminum has been registered as nearly 71.7 GPa. The shear modulus is 26.9 GPa (3900 ksi), as shown in Table 2. In general, this alloy is strong and resists deformation well, thus making it suitable for applications requiring a strong yet light metal. The tensile yield strength of 7075 aluminum alloy is 503 MPa, thus indicating that 503 MPa is the maximum stress a piece of this alloy can withstand without permanent deformation. These data indicate the excellent benefits of the alloying elements in 7075 aluminum, which make it suitable for structural materials such as aluminum tubing.

**Table 2.** Mechanical properties of aluminum alloy (AA7075) [13]

Ultimate Tensile Strength	572 MPa
Tensile Yield Strength	503 MPa
Shear Strength	331 MPa
Fatigue Strength	159 MPa
Modulus of Elasticity	71.7 GPa
Shear Modulus	26.9 GPa

The aerospace industry uses 7075 aluminum, although some fatigue failure can be detected. Because stress is cyclical, and therefore the material is periodically loaded with this force, micro fractures can appear after sufficient cycles of loading, thus weakening the material and eventually causing it to break. Because fatigue strength is a measure of the ability of a material to withstand cyclical loading, this parameter is useful for applications involving exposure to repetitive loading cycles, such as in aircraft or motor vehicles. The 7075 aluminum alloy has a fatigue strength of 159 MPa.

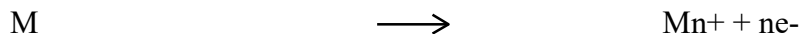
### I.3.3. Primary applications of aluminum alloy AA7075

The aluminum alloy AA7075 is used for highly stressed structural applications and has been extensively used in aircraft structural parts [14]. The first aluminum alloy X7075 was developed in secret by a Japanese company, Sumitomo Metal, in 1935 [3] but was introduced in the United States by Alcoa in 1943 and became standard in aerospace use in 1945[15]. Later, 7075 alloys were used for airframe production in the Imperial Japanese Navy.

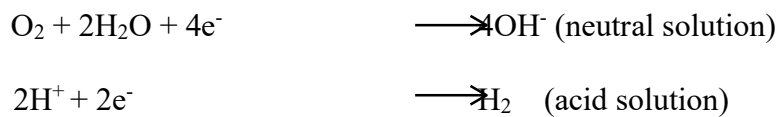
The 6061 aluminum alloy contains less zinc than the 7075 alloy. Whereas 6061 alloys provide superior welding abilities and workability, they lack the high strength and stress resistance of the 7075 alloy.

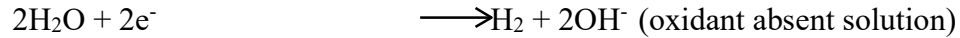
### I.3.4. Corrosion of aluminum alloys

Corrosion is a process occurring in most metallic compounds. Corrosion generally occurs when a metal or an alloy is exposed to an environment containing water and/or oxygen. Two coupled electrochemical reactions can usually be used to describe a corrosion mechanism. The first is the anodic reaction, in which the metallic atom tends to lose its electrons to form more stable oxide compounds [16]. The anodic reaction is depicted in the expression below [17]:



The second is the cathodic reaction, in which some absorbed chemical species from the aqueous solution obtain electrons via the metal surface. The typical reduction reactions occurring in neutral, acidic, or oxidant absent solutions are as following [15]:





For most metals, corrosion occurs spontaneously under most conditions, although the corrosion rates are variable and are significantly dependent on the metal activity and the environmental conditions. For example, magnesium is an active metal, and the oxidation of magnesium with oxygen or water occurs instantly. In contrast, the corrosion of steel usually occurs at a much slower rate. For some metal and its alloys, such as aluminum and stainless steel, a compact and stable passive layer can form over the surface and inhibit further metal oxidation. Therefore, passivation can inherently prevent the corrosion of some metals/alloys. At normal atmospheric pressure and temperature, in the absence of chloride ions, pure aluminum requires no corrosion protection [18]. However, corrosion easily occurs when two or more dissimilar metals are electrically combined as a galvanic couple and further exposed to a corrosive environment. The difference between the electrical potentials of two dissimilar metals makes the more active metal corrode at a higher rate.

Table 3 lists the galvanic series in which the tendency of a metal/alloy to corrode is shown in the sequence of activity in sea water. A metal preferentially oxidizes/corrodes if it is located at the top of the series, where the more active metals are situated. When two metals are coupled, the farther apart they are from each other in the series, the faster the anodic metal will corrode. Additionally, some metals such as aluminum can lose their passivation protection, owing to galvanic coupling with a nobler metal.

Copper, as illustrated in Table 3, is a more noble metal than aluminum. The copper-rich intermetallics in the aluminum-rich matrix act as a cathode, thus making aluminum the anode, which preferentially corrodes in a harsh environment. Consequently, aluminum oxidation



products accumulate at the interfaces along the grain boundaries. Therefore, the stress caused by the volume expansion of the accumulated aluminum oxidation products can break down the

---

**Table 3. Galvanic Series**

---

**Active End (Anodic)**

---

Magnesium

Magnesium Alloy AZ-31B

Zinc (hot-dip, dye cast or plated)

AA 1100-0

AA 7075 T-6

AA 2024 T-3

Steel 1010

Iron (cast)

Copper (cast, plated or wrought)

Nickel (plated)

Chromium (plated)

Stainless Steel 410 (active)

Silver

Gold

Graphite

---

**Noble End (Less Active Cathodic)**

---

Note: Adapted from Mulay, Master's Thesis, 2015.

grain boundaries and result in delamination and exfoliation, to a certain extent[19]. The corrosion reactions occurring in aluminum in an aqueous medium are shown in equations [20](1)–(3):

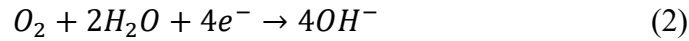
Anodic reaction:

Aluminum dissolution



Cathodic reactions:

Oxygen reduction on Aluminum in neutral or basic solution



Oxygen reduction on Aluminum in acid solutions



Both the anodic and cathodic reactions occur simultaneously in the corrosion process. The rate of oxidation and the rate of reduction are considered equal in a system. Therefore, owing to the electromotive force ascribable to the electrical connection between the Mg-rich primer and the aluminum substrate, an Al substrate/primer interface can be polarized to a mixed potential of the Mg particles/Al substrate. This mixed potential of aluminum substrate coated with Mg-rich primer has a cathodic potential value relative to the open circuit potential (OCP) of the aluminum substrate itself. Graphs of the OCP and potentiodynamic polarization depict the extent of the cathodic protection over the service time[20].

### **I.3.5. Coating technologies for prevention and control of corrosion of aluminum alloys.**

Multi-layer coating systems (coating + primer + topcoat) are a new coating technology used to protect aerospace aluminum alloys from corrosion in service. Traditional coating systems have been formulated containing hexavalent chromium Cr(VI) in both the conversion coating

and primer, volatile organic compounds (VOC), and hazardous air pollutants (HAP) in both the primer and topcoat [21]. In the same context, some heavy metals have been used for corrosion protection and to provide color. Environmental and health concerns are causing the aerospace industry to shift from using chromate conversion coatings and primers to using more environmentally friendly coating systems. Conversion coatings are thin, hydrated metal oxide films formed on a metal surface that ideally promote adhesion with primers, confer anticorrosion properties to the metal, and provide a reservoir of inhibitor ions during the coating lifetime [22] [23, 24].

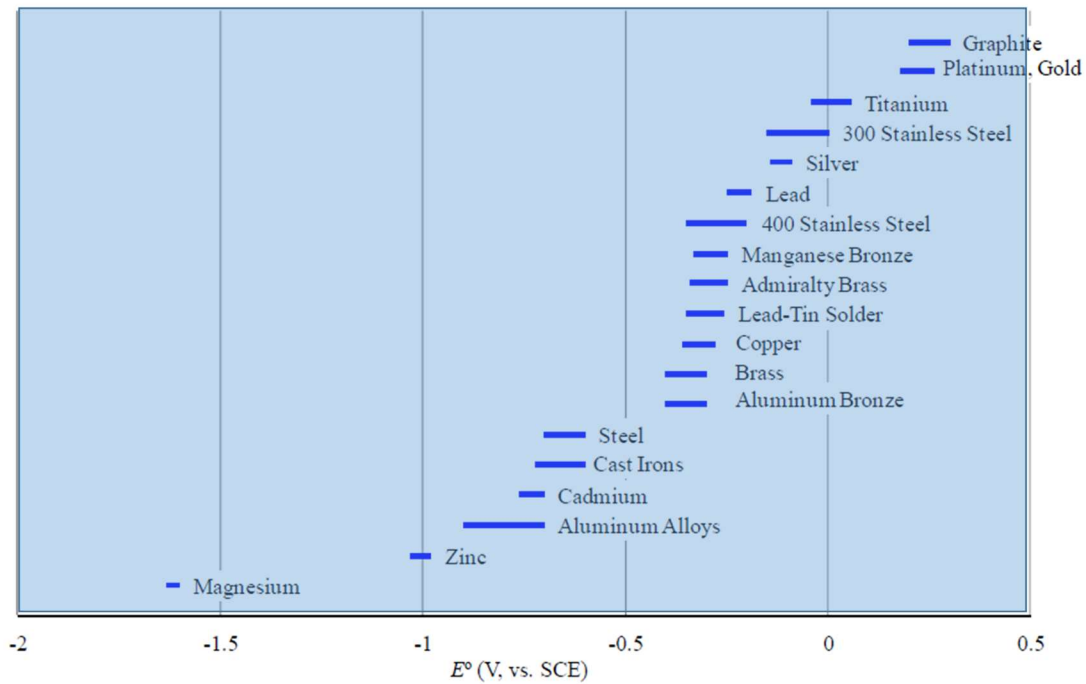
#### **I.4. Mg-rich Epoxy Coatings**

For many years, the technical performance of chromate coatings was used successfully. However, a recent approach uses a sacrificial metal-rich primer in the overall protection scheme; for example, zinc-rich coatings have been used to provide galvanic corrosion protection for steel substrates. In galvanic protection systems, the coating's metallic particles act as an anode (more negative electrical potential than that of the cathode) and are preferentially oxidized rather than the substrate.

The substrate acts as a cathode, owing to more positive electrical potential, and is protected against corrosion through the sacrifice of the anodic metal in the coating. Because magnesium is more anodic than aluminum and its alloys in the galvanic series, as shown in Figure 1, it is able to cathodically protect aluminum substrates.

When Mg-rich primers are formulated, small particles of magnesium metal are added at, or even beyond, the critical pigment volume concentration (CPVC). The high loading of

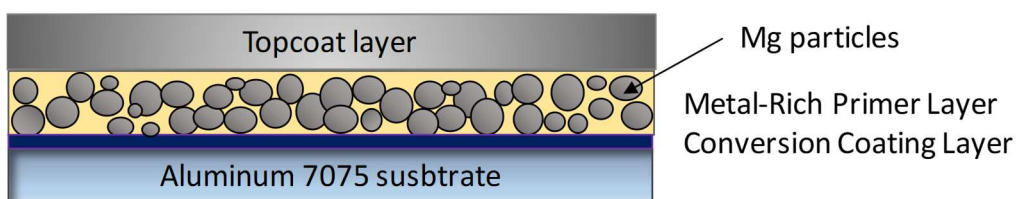
magnesium particles ensures that nearly all the metal particles are in electrical contact with one another and with the substrate. The electrical connection of metal particles is a critical requirement in this corrosion protective mechanism, thus establishing the anode/cathode relationship described above, as shown in Figure 2.



**Figure 1.** The electrochemical series versus the standard calomel electrode (SCE). Relative position between Magnesium and Aluminum alloys. Adapted from [DOD report- 2012-Price-WP-200731 Final Report-DOD-Magnesium Rich Primer Coating Technology]

In 2000, researchers at North Dakota State University (NDSU) developed the concept of a Mg-rich primer for cathodic corrosion protection of aluminum alloys without the use of chromate-based pretreatments or chromate pigments, analogously to the formulation of the Zn-rich primer coatings used in the protection of steel [20]. That research was enabled by the availability of

particulate Mg appropriate for use as a pigment in coatings. Whereas particulate Mg can pose a fire hazard, the thin layer of Mg oxide -4% wt.- on the Mg particles has been reported to stabilize bulk Mg against further oxidation [25]. Furthermore, natural Mg oxidation products are basic and therefore do not yield a sufficiently high pH to directly corrode and dissolve aluminum. Because Mg is more electronegative ( $-2.37$  V vs. SHE) than Al ( $-1.67$  V vs. SHE), the more noble Al substrate in this galvanic couple is cathodically polarized, whereas the less noble Mg particles in the coating matrix are anodically dissolved.



**Figure 2.** Schematic representation of metal-rich primers onto an aluminum substrate. [Report-2012-Price-WP-200731 Final Report-DOD-Magnesium Rich Primer Coating Technology].

The sacrificial action of Mg particles drives the electrical force in the protection process. The resulting protective cathodic current obtained through electrical contact of Mg particles inside the coating matrix is applied as the polarizing cathodic reaction for the aluminum substrate [20].

#### **I.4.1. Use of Mg alloys instead of pure Mg particles**

Three different Mg alloys were used as pigments in an epoxy-polyamide system studied by Xu et al. These alloys had different aluminum contents (5%, 8.5%, and 50%), and the pigments obtained were mixed with epoxy-polyamide at several PVC values [26]. The pigments of the alloys

were characterized as having large particle sizes of approximately 60 microns and different shapes. EIS analysis and SEM studies showed that the aluminum substrates obtained protection from the sacrificial Mg alloy pigments and from the precipitates formed during the oxidation of the Mg alloy particles, which were like those present in pure Mg-rich primers. In the same context, Bierwagen et al. have discussed the influence of the chemical compositions of two Mg alloy pigments, AM60 and AZ91B, and described the changes of the formulated coatings occurring through analysis with a Prohesion chamber [27]. For both these alloy pigments, XPS analysis elucidated a three-layer structure consisting of  $\text{MgCO}_3$ ,  $\text{MgO}$ , and metallic Mg, Al mixture, and ultimately a metallic core of Mg and Al. Below the critical PVC (CPVC), the main corrosion products were  $\text{MgAl}_2\text{O}_4$ ,  $\text{Al}_2\text{O}_3$ , and  $\text{AlOOH}$ . Above the CPVC, the main corrosion product obtained is  $\text{MgCO}_3$ . Below the CPVC, the DHS oxidizes first the Mg to  $\text{Mg}(\text{OH})_2$ , and then the Al to  $\text{Al}(\text{OH})_3$  when the pH increases. In the drying cycle, these products form  $\text{MgAl}_2\text{O}_4$ ,  $\text{Al}_2\text{O}_3$ , and  $\text{AlOOH}$ . Above the CPVC, the DHS penetrates the coating and neutralizes the zone around the Mg particles, while it is oxidized and maintains the pH low to prevent the oxidation of aluminum [20].

#### **I.4.2. Additional corrosion inhibitive components to improve Mg-rich performance**

The addition of small amounts of cerium oxide (0.5% by weight) to a Mg-rich primer was shown to significantly improve the protection performance of a Mg-rich primer on AZ91D magnesium alloy [20, 28]. Ceria particles did not change the protection mechanisms of the Mg-rich primer. However, the electrochemical activity of the Mg particles increased the service life of the Mg-rich primer. Apart from providing a barrier effect, ceria particles increased the corrosion potential and decreased the current density of the AZ91D alloy, which is beneficial for the

cathodic protection of the Mg particles. Lu et al. reported improved adhesion and better corrosion protection when the surface of AZ91D magnesium alloy substrates were coated with  $\gamma$ -glycidoxy propyl trimethoxy silane, due to the formation of Si–O–Mg covalent bonds between the silane film and the substrate and Si-O-Si bonds within the silane film, each shifting the water and oxygen permeability drastically [20, 29].

**Table 4:** Chronology Mg-rich primers.

2004	<p>NDSU developed prototype formulation [20]</p> <ul style="list-style-type: none"> <li>• Used 100+ <math>\mu\text{m}</math> Mg particles and a five-component resin system</li> <li>• Performed well in ASTM B 117 cyclic salt spray testing</li> <li>• ANAC licensed technology [30]</li> </ul>
2005-2007	<p>ANAC produced several experimental formulations (XP-406 and XP-417)</p> <ul style="list-style-type: none"> <li>• Used smaller Mg particle size, optimized pigment volume concentration</li> <li>• Lowered VOC levels</li> </ul>
2007-2008	<p>ANAC produced Aerodur® 2100 MgRP</p> <ul style="list-style-type: none"> <li>• Included orange pigment for contrast ratio, suspected of lowering corrosion performance</li> </ul>
2008-2009	<p>Re-baseline reformulation due to ESTCP lab results</p> <ul style="list-style-type: none"> <li>• ANAC produced Aerodur® 2100 MgRP 002</li> </ul>
2009-2012	<p>Improved corrosion performance, ESTCP-funded field testing delayed indefinitely</p> <ul style="list-style-type: none"> <li>• ANAC produced Aerodur® 2100 MgRP 003</li> </ul>
2012-2015	<ul style="list-style-type: none"> <li>• Magnesium-rich primer applied over AA2024 T-3 alloy exposed to aggressive environments</li> </ul>
2015-Present	<ul style="list-style-type: none"> <li>• Magnesium-rich primer/CNTs applied over AA7075 T-6 alloy</li> </ul>

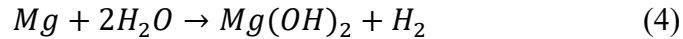
### **I.4.3. Multifunctional and hybrid coatings with carbon nanotubes (CNTs)**

Some coatings have been designed to provide an effective barrier inhibiting both inorganic corrosion processes through organic [31, 32], inorganic[33] [34], and hybrid approaches [35]; some coatings are environmentally friendly, thus avoiding environmental toxicity due to the use of inherently toxic formulations under aerobic or anaerobic conditions. Nano-hybrid coatings, also called nano-architected sacrificial coatings, have emerged as a new technology with dual protective mechanisms: 1) *Cathodic protection* achieved by integration of electrochemically active and sacrificial particles into the epoxy coating matrix, thus resulting in a galvanic effect, and 2) *Barrier protection*, a physical protection conferred by the polymeric matrix itself. New formulations including CNTs in hybrid metal rich multifunctional coatings are emerging; these have the advantages of improving the anti-corrosion properties by enhancing the physical barrier mechanism and cathodic protective effect [36]. The addition of nanostructures such as CNTs enhances both protective effects, thus allowing for better interconnectivity of Zn active particles by improving the electronic conduction of the epoxy matrix, owing to the high aspect ratio; these nanostructures also achieve a lower percolation threshold than other conductive particles, as described by Cubides et al., in zinc-rich epoxy primers containing multiwalled CNTs, with differing zinc content and fixed percentage of CNTs [36]. In same context, Park and Shon have demonstrated that increasing the content of multiwalled CNTs in epoxy coatings with different ratios of zinc dust results in higher conductivity, thereby improving the cathodic protection of carbon steel. Impedance measurements have confirmed the effects on corrosion protection [37].

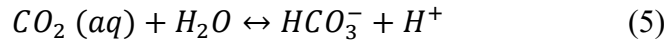


#### I.4.4. Factors influencing the behavior of Mg-Rich epoxy primers (MgRPs)

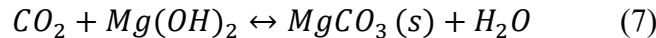
The authors reported a thin and porous magnesium hydroxide layer in Mg-rich primers exposed to salt spray. In contrast, a thicker, protective magnesium carbonate layer was detected in the samples when subject to natural weathering. The carbonate film was shown to inhibit both the anodic and the cathodic corrosion processes and does not result in blister formation. Consequently, Mg-rich primers exposed to natural weathering exhibit excellent corrosion resistance. However, salt spray conditions are not conducive to facilitate magnesium carbonate formation at a rate versus the rate of dissolution and corrosion [38]. Strekalov inferred that the amount of adsorbed water present on a magnesium surface at 95% relative humidity (RH) and 22 °C corresponds to more than 16 monolayers [39]. At very low concentrations of CO<sub>2</sub>, this adsorbed water will react with the surface film to form magnesium hydroxide, or brucite (Eq. 4).



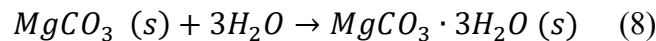
In the presence of CO<sub>2</sub>, protolysis of carbonic acid decreases the surface pH (Eq. 5 and 6)[40]:



Magnesium hydroxide is thermodynamically stable only at low CO<sub>2</sub> partial pressure and is converted into magnesite (MgCO<sub>3</sub>) in the presence of atmospheric levels of CO<sub>2</sub> (Eq. 7) [41, 42].



At high RH, magnesite forms a stable, hydrated magnesium carbonate, i.e., nesquehonite (Eq. 8).



Equations 4–8 support the explanation why Mg(OH)<sub>2</sub> was not transformed into magnesium carbonate in Mg-rich primers at the relatively low CO<sub>2</sub> content in the salt-spray chamber

environment as well as primer film exposed to humid environments in glass jars. The relative proportions of magnesium hydroxide and magnesium carbonate are influenced by CO<sub>2</sub> concentration (the salt-spray chamber has less CO<sub>2</sub> than field exposure), CO<sub>2</sub> solubility (in water/salt water)[43], and chloride [44].

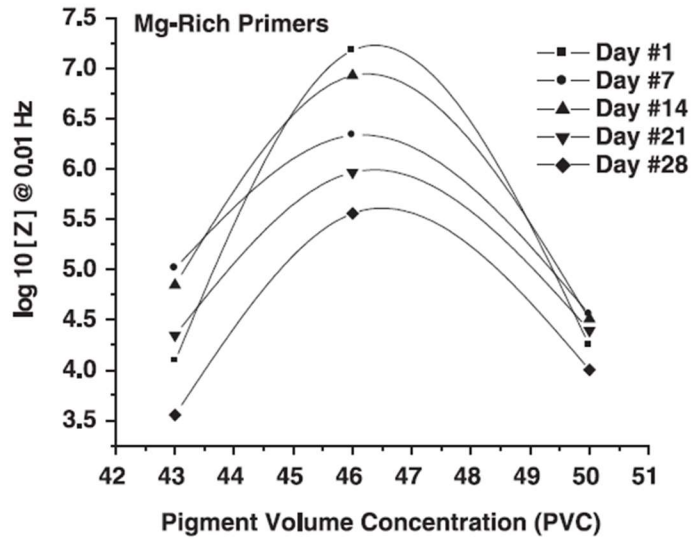
#### **I.4.5. Techniques for performance evaluation of Mg-rich epoxy coatings**

The Mg-rich primers applied on aluminum alloys have shown outstanding performance in outdoor exposure at various sites across the US in a wide range of applications. The excellent performance of Mg-rich primers has been demonstrated depending on multiple factors including a) the polymer properties, b) Mg PVC, c) the type of Mg particle (pure Mg, Mg alloy, or Mg particles with an oxide/hydroxide/carbonate layer), and d) the environment. Many interesting electrochemical studies have used methods such as electrochemical impedance spectroscopy (EIS), potentiodynamic polarization, scanning electrochemical microscopy (SECM), and OCP to elucidate the protective mechanism provided by Mg-rich primers on aerospace-grade aluminum alloys. Most of these studies have suggested that the observed cathodic protection is provided by the uniform corrosion/dissolution of the Mg particles in coating matrix[20].

#### **I.4.6. Electrochemical impedance spectroscopy to study the electrochemical behavior of Mg-rich epoxy primer**

Electrochemical impedance spectroscopy (EIS) is a technique that can be used to describe the electrochemical behavior of coatings, and a useful method for studying, measuring, and estimating coating durability [45-51]. EIS is a non-destructive technique that provides quantitative results and is sufficiently sensitive to investigate the deterioration of coating on a

metal. This method can be used for determining coating performance and the protective mechanism. Some electrochemical elements associated with the corrosion process, such as coating capacitance, coating resistance, double-layer capacitance, and charge transfer resistance, can be determined via superposing experimental data and the results from equivalent electrical circuit (EEC) models.



**Figure 3.**  $|Z|$  modulus at 0.01Hz vs. PVC for Mg-rich epoxy/polyamide primers at pH = 6.2 in 3% NaCl [Nanna, 2004 ----Ellingson, L., “Corrosion Studies of the Protection of Aluminum Alloys and Outdoor Bronze,” Masters Thesis, North Dakota State University, June, 2001.]

Figure 3 shows the low-frequency impedance modulus  $|Z|$  versus the exposure time measured in 3% NaCl solution at pH = 6.2 on 43, 46, and 50% PVC Mg-rich primers. This primer was applied onto aluminum T2024 for 28 days [25].

## **I.5. Stainless steel**

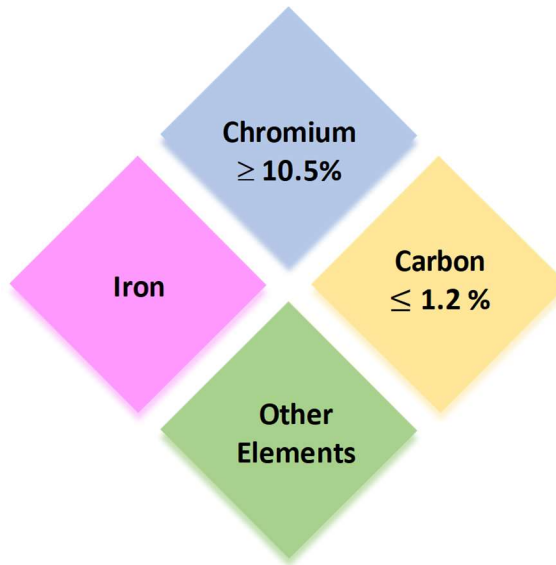
Stainless steel is an extremely useful corrosion-resistant alloy constituted by iron, chromium, and sometimes nickel and other metals, as illustrated in Figure 4. Stainless steel is considered an excellent non-corrosive material to date. In the construction sector, it is considered to have a recovery rate close to 100%. Stainless steel is also considered environmentally neutral and inert, and therefore its long-life extension limits the need for sustainable construction. Furthermore, it does not promote the dissolution of elements that could modify its composition in contact with aggressive anions. In addition to these beneficial environmental characteristics, stainless steel is aesthetically appealing, hygienic, and exceptionally durable. It is used in several industries, including energy, transportation, building, research, medicine, food, and logistics. The unique properties of stainless steel conferred by the presence of chromium in the alloy are presented schematically in Figure 5, which illustrates the passive layer that allows the steel to resist the corrosion process.

### **I.5.1. Types of stainless steels**

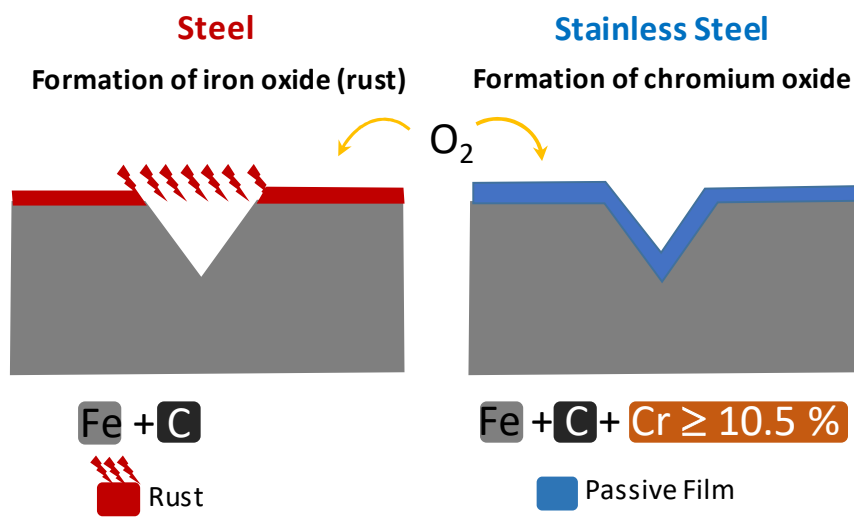
There are three main types of stainless steel: ferritic, austenitic, and martensitic. This classification is based on composition and structure. Stainless steel is based on the binary Fe-Cr system, which is modified by the addition of specific alloying elements, which influence the material's microstructure and physical properties.

#### *a) Austenitic S300*

Austenitic S300 steel contains approximately 0.015 % carbon, 18 % chromium, 15 % nickel, and sometimes 7% molybdenum. The presence of nickel tends to improve the corrosion



**Figure 4.** General chemical composition of stainless steel [52]



**Figure 5.** Schematic distinction between steel and stainless steel [52]

resistance in certain media and to increase the ductility of stainless steel. Molybdenum enhances the resistance to corrosion in an acidic media. Most common grades of austenitic steel are 304/304L and 316/316L. This material is important in boilers, aeronautic applications, electronic

components, railway equipment, tubes, chemical tanks, food vats, marine applications, heating systems, resistor jackets, and furnace equipment.

*b) Austenitic with Manganese (200 series)*

Austenitic with manganese (200 series) steel has chromium, manganese, and a low concentration of nickel content (consistently below 5%). This material is used in asphalt tankers, tubes, and food containers.

*c) Ferritic*

The ferritic steel chemical composition is 0.02% carbon, 10.5% chromium, and 4% molybdenum. It is used in high temperature applications, because of the stability of the tensile property and resistance to fatigue. This type of steel is magnetic. structural products. It is used in car exhaust systems, conveyor chains, cooking utensils, boilers, domestic appliances, trim, dishware, heating, and hot water tanks.

*d) Duplex*

The chemical composition of duplex steel is 0.02% carbon, 0-4% molybdenum, 1-7% nickel, and approximately 21% chromium. These stainless steels possess a two-phase microstructure consisting of grains of ferritic and austenitic stainless steel. Duplex stainless steel is approximately twice as strong as austenitic or ferritic stainless steels because of its low nickel content. Applications include oil, gas, pulp and paper, desalination and chemical industry.

*e) Martensitic*

The chemical composition of martensitic steel is approximately 0.1% carbon and 10.5-17% chromium. Martensitic steel is structurally similar to ferritic stainless steel; however, sometimes contains high carbon concentrations (>1.2%). Common uses are surgical instruments, cutting tools, and hand tools. These alloys are designed to resist the effects of corrosion and heat.

### **I.5.2. Coatings design for stainless steel**

Corrosion in steel cannot be avoided entirely. Nonetheless, it can be partially prevented through various corrosion mitigation technologies such as design improvement, coatings, corrosion-resistant alloys or composites, cathodic and anodic protection, or corrosion inhibitors. Different materials such as nitrides, transition metal oxides, polymers, nanoparticles incorporated matrices, and organic metals, have been used as protective coatings on metal surfaces to prevent corrosion [53-60]. Among these materials, thin films of TiO<sub>2</sub> have been widely used, as they provide improved wear resistance, hardness, and high corrosion resistance [61-65].

Nanocomposites of titania such as CeO<sub>2</sub>/TiO<sub>2</sub>, TiO<sub>2</sub>/CuO, TiO<sub>2</sub>/SiO<sub>2</sub>, and titanium incorporated polymers, among others, have been produced and studied in the past [14–17]. Nanocomposites of ZnO/TiO<sub>2</sub> have a wide range of applications in fields including photocatalysis, dye-sensitized solar cells, humidity, and gas sensors. [18–21]. However, a detailed survey of the literature suggests that anticorrosion studies of nanocomposites of TiO<sub>2</sub> and ZnO have scarcely been attempted. Thin films of zinc oxide and titanium dioxide have been deposited by a variety of techniques such as anodic deposition, chemical vapor deposition, RF magnetron sputtering, atomic gel epitaxy, electron beam evaporation, sol-gel technique, electrochemical deposition, and thermal evaporation [22–26]. Spray pyrolysis is an economical method for coating materials for various applications. However, the requirement of high temperature for substrate heating (500°C–800°C) is a major shortcoming of this method. The spray coating of pre-synthesized nanoparticles or nanocomposites provides an alternative route to prepare anticorrosive coating on steel substrates.

## CHAPTER II

# ELECTROCHEMICAL INVESTIGATION OF THE SYNERGIC EFFECT BETWEEN MAGNESIUM PARTICLES AND CARBON NANOTUBES IN EPOXY COATING

### II.1. Introduction

Magnesium-rich primers (MgRP) have been developed by several groups [25, 27, 66-71]. One classical work by Bierwagen and colleagues [72] has used these primers to protect aluminum alloys. They have described how the efficiency of the sacrificial protection of MgRP depends on several aspects, such as the physical contact between the aluminum surface, the magnesium particles, and electrolytes. King and Scully[73] have suggested two possible modes of protection of MgRP: magnesium particles with adequate connection protect remote defects, and the Mg pigments that remain isolated protect local defects. Both modes of protection depend on the electrical resistance of the primer, which is a function of the pigment volume concentration (PVC). The PVC affects the resistance of the path between the particles, the aluminum substrate, and the resistance of the coating to electrolyte penetration [74]. Previous research has demonstrated that the primer connectivity depends on the magnesium content. The critical pigment volume concentration (CPVC) marks the transition from non-conductive to conductive behavior. Variations in CPVC depend mainly on particle alignment, which in turn depends on the particle shape and particle size. Xiangyu et al. [69, 75] have found that when the amount of magnesium particles increases, the electrochemical cathodic protection effect also increases. However, the pore resistance decreases when the content of magnesium increases. The authors have suggested a three-stage mechanism: electrolyte permeation through the coating, cathodic protection, and formation of Mg corrosion products.



Additional fillers, which diminish the electrical resistance of the coating [27, 28], are necessary to enhance the connectivity of the primer to improve its cathodic protection effect and decrease the porosity of the binder [76]. Carbon nanotubes (CNTs), which are inert chemical particles, interconnect magnesium particles, owing to their high surface area. Cubides et al.[35] have performed a comprehensive study investigating the influence of CNTs on the efficiency of the sacrificial effect of the active particles within the coating. They have defined the interconnectivity of the CNTs and how CNT addition influences the barrier effect in water uptake. They have found that the sacrificial effect is more effective in the presence of interactions between particles and conductive nanowires or CNTs.

Turhan et al. [77] have reported that adding CNTs to pure magnesium increases the corrosion rate, owing to the higher cathodic activity. The corrosion rate depends on the dispersion level of the multiwall CNTs (MWCNTs). MWCNT dispersion produces a homogeneous coating with a thinner corrosion product layer. This thin oxide layer does not protect the surface of the multifunctional composite. Jingrong Liu et al. [78] have determined that addition of single-layer graphene promotes the formation of zinc oxide structures at the coating/substrate (steel) interface. The graphene accelerates the electrochemical reaction between the active zinc particles and the steel substrate. The corrosion products formed at the steel surface increase their impedance over time because of the barrier effect.

Prior work has demonstrated that CNT addition may have two different effects on MgR coatings. The first effect is an increase in the Mg particles' reaction kinetics in the epoxy, owing to better interconnectivity between active particles and regions where the corrosion products are unstable. This increase influences the cathodic protection efficiency of the initial process, owing to higher current protection, while a homogeneous distribution is present along the substrate

surface. Although the magnesium particles embedded in the coating are used more efficiently for the cathodic protection effect, the protection period probably decreases in the presence of CNTs, which impede the formation of stable corrosion products among the Mg surface particles. The decrease in the stability of the corrosion products could affect the barrier effect and the second control mode. The classical physical barrier properties exerted by the coatings in combination with a galvanic sacrificial anode extend the life of the alloy against corrosive environments. Because aluminum is at a low position in the galvanic series, it must be protected by a more active material. Hence, magnesium-enriched coatings are suggested for the protection of such alloys. The present research aims at characterizing an MgRP applied on Al 7075 substrate. The balance between the barrier effect and the sacrificial effect was shifted because of the CNT content. EIS was used to characterize the interfacial mechanisms existing at the different particle/epoxy interfaces. The coating characteristics were varied on Al 7075 T-6 substrates to compare the responses of the interface and to study the existing transport mechanism of the coating layer. The interfacial reactions were studied to determine the corrosion mechanism within the formed layer on the basis of the damage evolution concept. The electrochemical characterization of the system was performed by monitoring the coating/substrate/electrolyte interface in real time. Multi-scale theoretical tools, comprising electrochemical testing techniques, high surface resolution techniques, and characterization methods, were used to analyze the performance of the substrate/coating interface according to the physical characteristics (thickness and environment) of the primer layer.

## **II.2.Experimental procedure**

### **II.2.1. Electrolyte solution**

The electrolyte used for this test simulates a neutral media. All the chemicals used are analytic grade, and the water was deionized to high purity. For preparing 200ml of a 0.2M phosphate buffer, it is necessary to mix a sodium dihydrogen phosphate solution and a sodium dibasic phosphate solution. The monobasic solution (0.23M) was made with 2.78g of sodium dihydrogen phosphate dissolved in 100 mL of distilled water. For the dibasic sodium phosphate solution (0.37M), 5.3 g of disodium hydrogen phosphate was dissolved in 100 mL of deionized water. After that, 39 mL of dihydrogen sodium phosphate solution are mixed with 61 mL of disodium hydrogen phosphate solution. This later mixture is made up to 200 mL with distilled water. As a result, this gives a phosphate ( $\text{PO}_4$ )<sub>2</sub> buffer solution 0.2M [33].

### **II.2.2. Coated samples**

The magnesium-rich coating consisted of a solvent-based two-component epoxy-polyamide primer that contains magnesium particles. For the preparation of the primer, different volume percentages of magnesium particles (15%, 30%, and 60% PVC) of 50 $\mu\text{m}$  average size were gradually added to the epoxy resin (Tesla P1150ASAS) and mechanically stirred at room temperature forming a homogeneous mixture. Then, a stoichiometric amount of hardener (Tesla P1150BSAS) with a weight ratio (epoxy resin: hardener) of 2:1, was incorporated into the mixture and sonicated for 5 min. The magnesium particles are usually covered with a thin layer of MgO that controls the reactivity of magnesium under dry conditions.

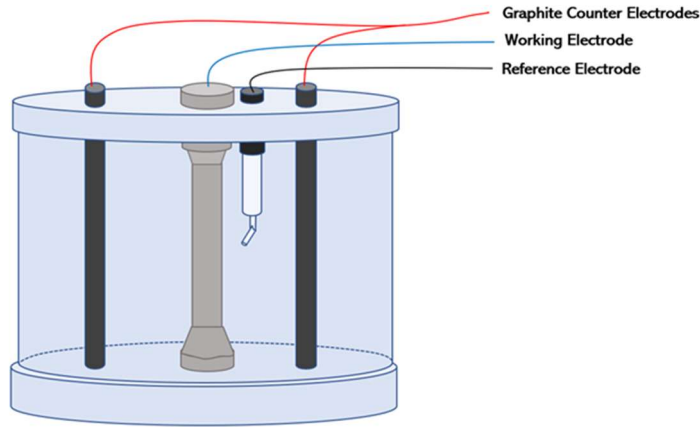
The coatings that contain CNTs, the epoxy resin was mechanically mixed with 0.77 wt% of CNT until they got entirely dissolved. Then a percentage of magnesium particles was gradually added to the mixture while stirring at room temperature. Then, the hardener (in the same proportion with no nanotubes) was incorporated into the mixture and sonicated for 5 min.

Al 7075 T6 cylindrical test specimens were sprayed with the prepared formulations. The dimensions of the cylindrical test specimens are selected according to standard ASTM E8/E8M samples. Prior to the application of coatings, the aluminum specimens were degreased with acetone and dried at room temperature. The coated systems were allowed to cure for 6 hours at 60°C and kept at room temperature for seven days before being exposed to the electrolyte.

### **II.2.3. Electrochemical measurements**

The Electrochemical measurements were conducted using a Gamry Reference 600+ Potentiostat/Galvanostat/ZRA. The tests were carried at room temperature in a three-electrode cell setup. The reference electrode used in the test is a saturated calomel electrode (SCE); the aluminum rod, magnesium rod, and aluminum-coated samples served as the working electrodes, and two graphite rods were utilized as counter electrodes as illustrated in Figure 6.

The experimental test involves a sequence that includes Open Circuit Potential (OCP) and EIS measurements on the cylindrical specimens exposed to a buffer solution at constant pH = 7. EIS parameters were set for a frequency range from 100 kHz to 10 mHz with a voltage amplitude of 10 mV. The electrochemical cell was filled with the electrolyte solution for the duration of the experiment (28 days). The exposed area of the working electrode was 8.0 cm<sup>2</sup>.



**Figure 6.** Experimental set up.

#### **II.2.4. Materials characterization**

The cross-section of the samples with different compositions of magnesium particles and CNT were characterized by a scanning electron microscope (SEM, JEOL JCM-600 Plus) equipped with energy-dispersive X-ray spectroscopy (EDS) function before and after the immersion tests. The SEM visualized the structural changes of the coating with a distribution of magnesium particles before and after the immersion, and the EDS revealed the modifications in elemental composition, especially the magnesium particles, due to the immersion testing. The samples were epoxy-mounted and then grounded by with 240- to 800-grit SiC paper to perform for the cross-sectional imaging. Then the samples were subsequently polished by 9-, 3-, 1-, and 0.05- $\mu\text{m}$  diamond suspension using a polishing cloth and finished by ethanol cleaning. The samples were coated with 2 nm thickness Pt coating to minimize surface charging.

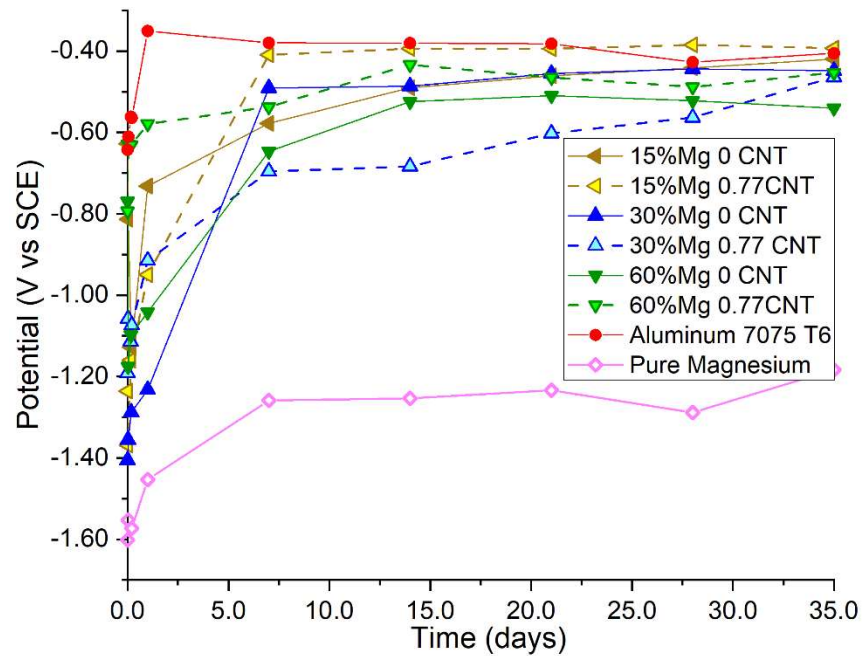
## **II.3.Results and analysis**

### **II.3.1. Open circuit potential (OCP)**

Figure 7 shows the change in open circuit potential (OCP) for the coatings containing different amounts of Mg particles in the presence or absence of CNTs. On the basis of comparison with the OCP of the substrate without the coating, which is shown as a reference, the presence of cathodic protection was observable by means of the added Mg particles, which served as a sacrificial anode, particularly during the early period of immersion. The OCP values decreased when the Mg particles were added to the coating matrix, thus revealing the contribution of Mg particles according to the mixed potential theory [15]. In addition, increased amounts of Mg particles provided more extended cathodic protection, as observed as a relatively slower transition of the OCP toward more positive values over time.

In the presence of CNTs, considerably faster OCP changes to more positive values were observed in the early period until day 5. This finding was potentially produced by the CNTs, which facilitated the transfer of electrons by providing a conductive path throughout the coating matrix [72]. Therefore, more Mg particles were activated and allowing for rapid exhaustion of the cathodic protection in the case of the 15% Mg and 0.77 CNT sample, which contained limited amounts of Mg. In contrast, the higher Mg content of 30% Mg and 0.77 CNTs resulted in a relatively slower OCP increase, thus indicating longer cathodic protection. This finding was attributed to the abundance of Mg particles throughout the coating matrix and the increased conductance produced by CNTs, which enhanced the utilization of the Mg particles. Our findings suggest an increase in the cathodic protection range when more Mg particles can potentially serve as sacrificial anodes and consequently increase the cathodic protection period.

At 30% PVC, the initial transient for the first hour included a potential of -1.4 V vs. SCE, which changed to -1.28 V vs. SCE. The magnitude was lower than the aluminum potential; consequently, magnesium particles exerted cathodic protection during the exposure time. At 42 days, a small decrease in potential was observed with respect to the bare aluminum sample. The change in potential over time was influenced by the particle's distribution within the epoxy matrix. This effect also contributed to the particles' surface wetting and activation or surface



**Figure 7.** OCP evolution for different Mg and CNT concentrations exposed to buffer solution at pH=7

reaction. The addition of CNT to the polymeric matrix caused the surface to show a weaker polarization response after exposure. The OCP magnitude rapidly changed after a week of exposure, from a magnitude of -1.15 V vs SCE to -0.7 V vs SCE, and the change was slower thereafter. The initial change was attributed to the activation of the MgR particles distributed within the polymeric matrix, and the slower change in the presence of CNTs was attributed to the

interconnectivity between particles, thus improving the efficiency of the particle surfaces through greater surface wetting.

At 60% PVC, the magnitudes were less negative than at 30% PVC; the potential was initially -1.22 V vs SCE, then changed to -0.68 V vs SCE after a week of exposure. The potential values were subsequently stable (approximately -0.52 V vs SCE). The cathodic protection was active during the entire exposure time. The addition of the CNT particles produced a similar effect to that with 30% PVC; the potential magnitude was more positive, and the gradient was not as stepped as that with 30% PVC.

Several circumstances might have affected the potentials of the samples during the first days of immersion. First, the magnesium particles added to the composite coating already had an oxide or hydroxide layer formed. Magnesium is highly reactive to oxygen and humidity [xx]. This oxide/hydroxide layer might have dissolved in the initial immersion, thus allowing the most negative potentials to be reached after 1 hour. After this dissolution process, the magnesium particles developed a new oxide/hydroxide coating on their surfaces, owing to the interaction with the testing electrolyte and the oxygen dissolved in it.

The coatings with fewer magnesium particles (15% Mg) showed faster changes to positive potentials than those with a greater amounts of magnesium. The lower amounts of magnesium particles, compared with higher amounts, were less able to retain a more negative potential after formation of the “new” oxide/hydroxide coating. A higher amount of magnesium particles was able to address a more negative potential for longer periods of time.

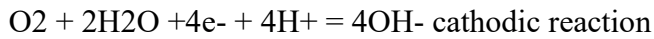
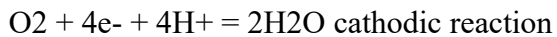
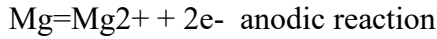


## **II.3.2. Mg content influence on the evolution of corrosion control performance**

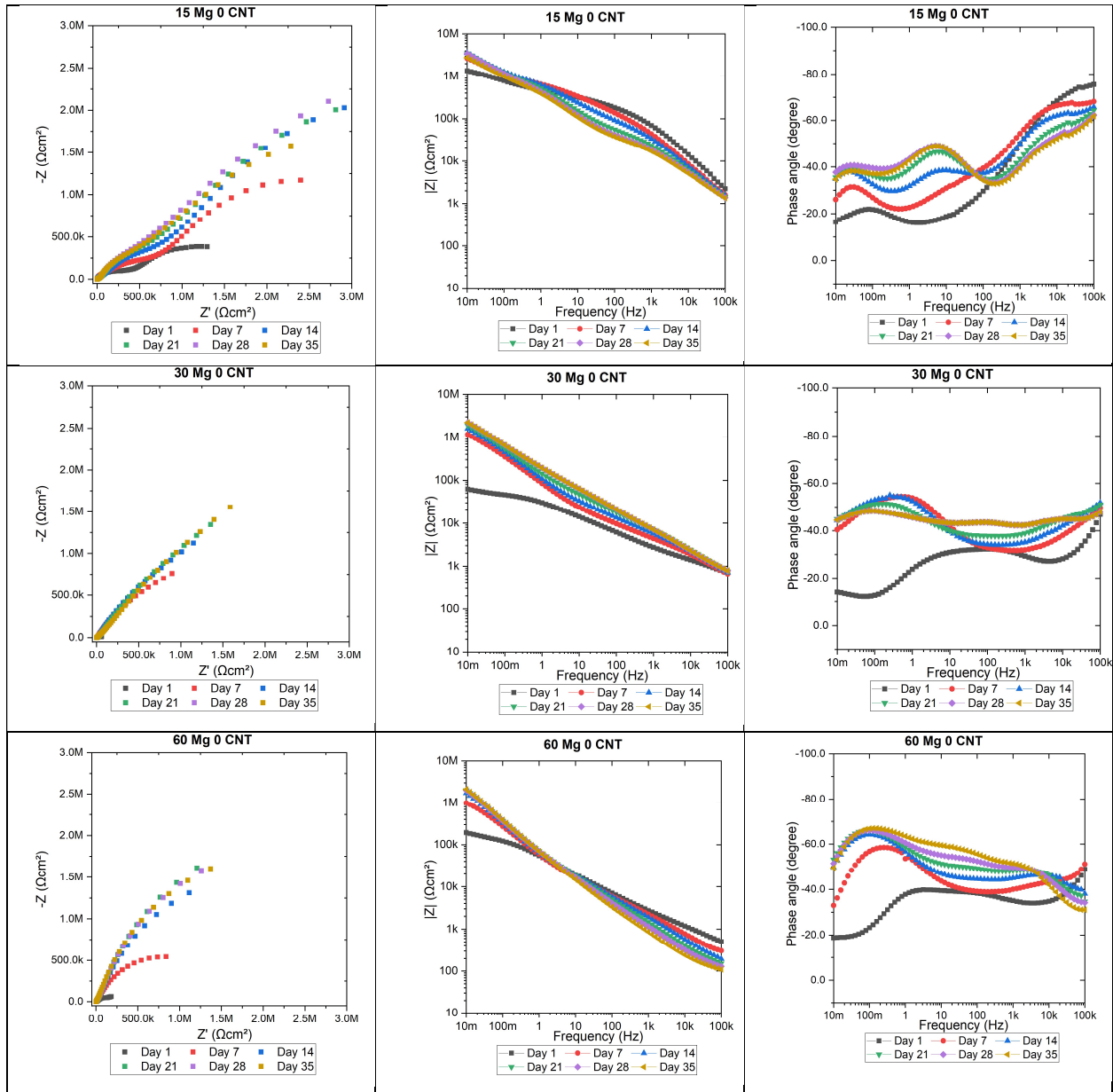
### **II.3.2.1. MgR 15%**

Figure 8 shows the EIS evolution for 15% Mg with different immersion times. The composition of the MgR epoxy showed different time constants during the entire immersion test period. Through impedance spectra, we identified three different stages during the entire immersion time: the activation stage, involving the water uptake of the electrolyte within the polymeric matrix; the active to passive stage due to the wetting of the particles influencing the particle reactions; and the passive or steady state stage following the coverage of the active surface. The complex representation included a loop at high frequencies, such that the second time constant was associated with the second loop illustrated in the complex diagram, and the third loop appeared at low frequencies. The phase angle representation presented time constants with a clearer appearance and evolution, owing to the maximum magnitudes displayed at different frequencies. Previous work by Scully and Bierwagen [xx] has demonstrated the contribution of MgR particles integrated in the polymeric matrix on aluminum substrate and the water uptake and the surface reaction. The initial stage for the MgR involved the wetting or water uptake process in the epoxy binder; after day 1, the complex representation indicated the contribution of the MgR particles at medium frequencies. The presence of Mg particles resulted in an initial chemistry with oxide formation or active surface sites. The phase angle displayed an increase in terms of the maximum magnitude. The third maximum in the phase angle representation was characteristic of a time constant, which resolved the characteristics of the particle/epoxy interface. At the initial stage, we observed two different time constants for the polymer matrix and the particle reactions at the interface. The electrolyte reached the surfaces of

the Mg particles, and electrochemical reactions occurred; the magnitude of OCP reflected the interaction of the particles, with the electrolyte having a negative value at the initial time. Both electrochemical reactions included the dissolution of magnesium and the oxygen reaction as the cathodic reaction. Previously, Scully et al. reported the reactions of MgR particles with an NaCl electrolyte as follows [xx]:



The initial stage involved a combination of water uptake and activation of particles during the first 7 days. Starting on the 14th day, an additional time constant appeared, thus marking a different stage, in which the particles formed a passive layer of corrosion products from the activation state. The OCP is an additional indicator of the active to passive transition stage. The resistance of the coating continued to decrease, and its capacitance increased because of electrolyte permeation and particle surface reactions. The distribution of the Mg particles in the polymeric matrix after exposure to the electrolyte for 7 days indicated an increase in the phase angle, which was associated with the time constant appearing at medium frequencies, owing to an increase in the thickness of the passive layer that formed and surrounded the magnesium particles. The magnesium particles continued to react after 14 days. Simultaneously, the thickness of the passive layer continued to increase until reaching a steady state or saturation stage. The passive state of the particles reached saturation at 21 days, the phase angle at mid frequencies remained constant, and the OCP also showed a plateau in magnitude. The Mg at this percentage was distributed and embedded along the polymeric matrix and showed a time response to the electrolyte. Owing to electrolyte uptake, the pathways, the distribution set



**Figure 8.** EIS Nyquist and Bode plots for Mg-rich primer-aluminum system without carbon nanotubes

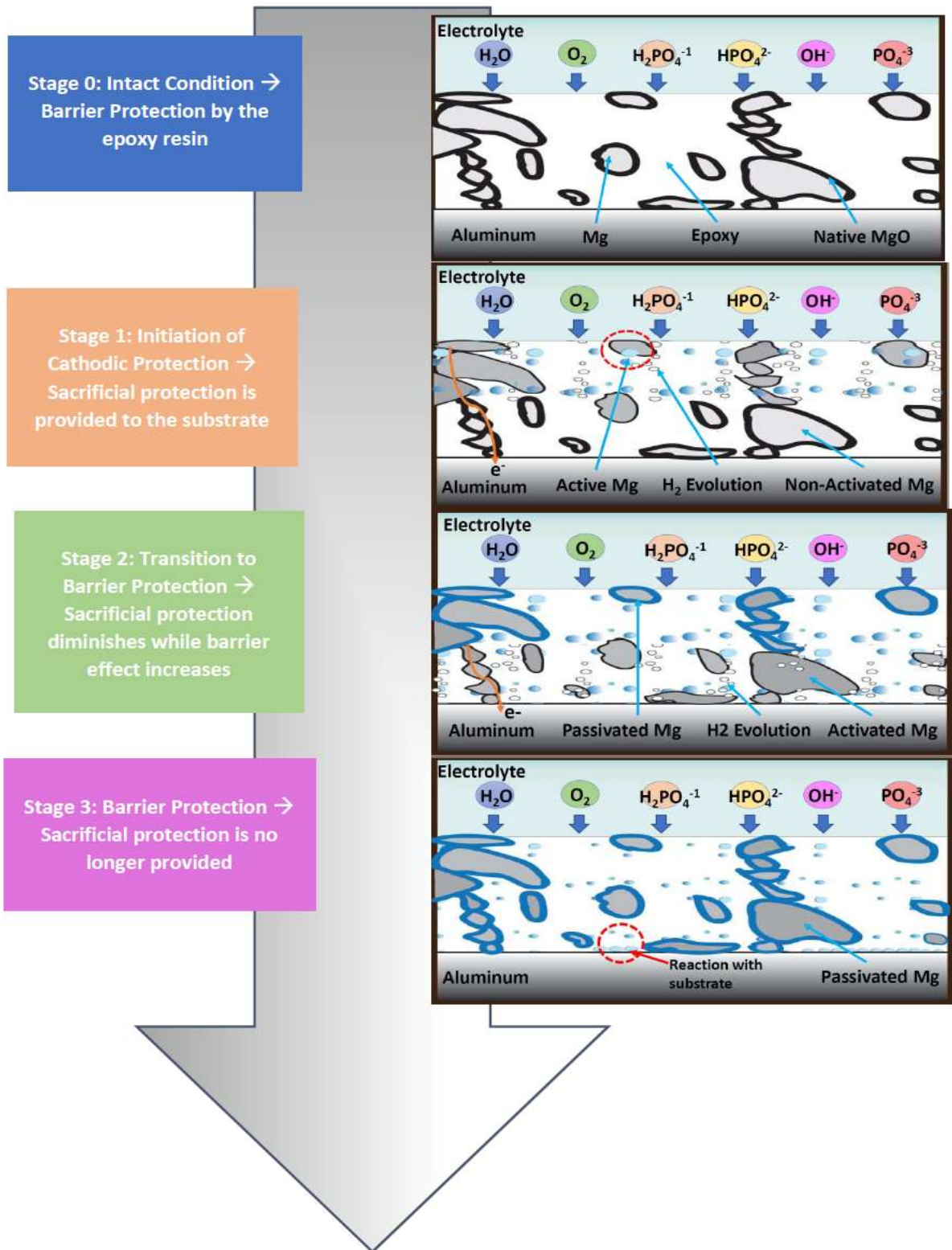
different surface conditions, after 21 days, the electrolyte had reached all sites potentially available for direct electrochemical interaction. The second stage was passivation of the particles until steady state. After the passive state, no further effects were observed at the interface. The

open circuit at this concentration of magnesium particles remained at a magnitude that no longer indicated a sacrificial effect; thus, the conditions were suitable for barrier protection, as showed in Figure 9. Several studies have assumed that the sacrificial effect for MgR epoxy on aluminum acts at certain magnitudes. In this work, after 21 days, the electrolyte continued to permeate the coating, as represented by a continuous decrease in its coating resistance.

#### **II.3.2.2. MgR 30%**

The corrosion degradation mechanism for this MgR formulation is defined in three stages. In the first stage, the phase angle shows three time constants associated with the polymer matrix, the particle characteristics, and the interface between the particle and polymer. The first apparent difference between this formulation and the previous formulation was the rate change in the time phase EIS response and the magnitudes of each time constant; the OCP was consistent with the initial activation stage producing a large potential change from day 1. Figure 8 shows the first day of immersion, and the impedance spectra show a phase angle magnitude and a continuous decrease at high frequency, possibly because of the higher conductivity materials within the polymeric matrix. The water uptake and activation in the initial stage were influenced by the higher Mg concentration and greater particle/particle contact. The activation stage occurred after day 1 because of the galvanic action produced by the particles with the substrate.

A mid-frequency time constant appeared after 1 day and increased in magnitude, thus influencing the passive stage of the particles. The second stage was observed through not only the formation of corrosion products and accumulation in the particles, but also the phase change at low frequency. This finding indicated the interface between the particle and polymeric matrix according to the electrochemical reactions described earlier. After 7 days of exposure, the EIS.



**Figure 9.** Proposed mechanism of protection conferred by the 15% Mg coating.

response characterizing the second stage showed an increase in the mid frequency phase angle from 35 degrees to 45 degrees. Previous work [xx] has demonstrated an accumulation of corrosion products and a decrease in capacitance; in this case, the CPE denotes denser material, and the formation of Mg oxides and hydroxides [xx] describes the nature of the semiconductor formed. The low frequency considers the charge transfer and CPE associated with the double layer at the particle-polymer interface. The formation of a time constant at low frequencies indicates the activity of the area available for electrochemical reactions. In the last stage of exposure time, the passive stage for this MgR composition was characterized by the formation of precipitates and corrosion products, and the depletion of the active surface resulted in more favorable kinetics, owing to the initial active area. The third stage was identified at 21 days, when no further change in each of the time constants along the frequency range was observed. The phase angles showed an almost horizontal line across the frequency range, with a small indication of a time constant at high, medium, and low frequencies; this finding might have been due to the saturation of the MgR particles within the polymeric matrix. The distribution might have occupied the coating volume, and the contact surface between particles was higher than that with 15% MgR. The phase angle remained at 42 degrees after the 42 days, and the OCP was stable at -0.48 V vs SCE at the end of the exposure time and did not exceed the threshold at which cathodic protection would have an effect. Instead, the barrier protection was a more dominant mechanism. The corrosion products and the particle distribution influenced the passive stage in the presence of this formulation

### **II.3.2.3. MgR 60%**

Figure 8 shows the impedance results for the MgR60 at different exposure times in the pH=7 buffer solution. The presence of the highest content of MgR particles (60%) resulted in

similar evolution processes to those observed with the previous two concentrations, according to the EIS signatures. Some important differences with respect to the previous formulations should be noted. We were able to distinguish the water uptake and activation stage after 1 day of exposure; the phase angle at the highest frequency showed a decreasing maximum point with respect to time. The Mg content influences the particle contribution to the conductivity and porous distribution. In the initial stage, during the first 7 days, the electrolyte uptake by the polymer matrix and the activity of particles produced the first two-time constants observed with the previous two Mg compositions. The second stage involved an active to passive transition, in which the particle surfaces reacted and began to form corrosion products. The time constant at medium frequencies appeared at day 7 and increased thereafter. The higher particle content provided more active sites for the electrochemical reactions. The particles distributed along the polymer, and the interconnectivity between particles was greatest at that point. The OCP showed a greater positive magnitude than that observed with 30% MgR. This finding was not expected when we considered the proportionality between the content and active surface. However, the polarization rate showed a less stepped slope than that of the previous composition, because the particle distribution produced more sites available for electrolyte uptake; the particle to particle or particle alone could have a larger area and a smooth active to passive transition. The phase angle at mid frequencies and low frequencies showed particle reactions due to the continuous accumulation of corrosion products. Each time interval of 7 days showed the same increase for the phase angle in mid frequencies. The low frequencies revealed an increase in the charge transfer and phase angle; the latter effect was attributed to the decrease in the active sites and the increase in passive or corrosion product coverage. The third stage was assumed to exist after 42 days of exposure. The phase angle magnitudes did not change significantly at that point. The

phase angle magnitude was highest at mid and low frequencies, at 62 and 70 degrees, respectively. In addition, the OCP was negative after the longest exposure time with respect to the aluminum threshold between galvanic and sacrificial protection. The composition influenced the performance of the MgR epoxy content. The distribution of particles was not controlled or monitored after the sample preparation, and the process was performed in the same manner. The distribution could be studied by the addition of CNTs and by considering different stages during immersion.

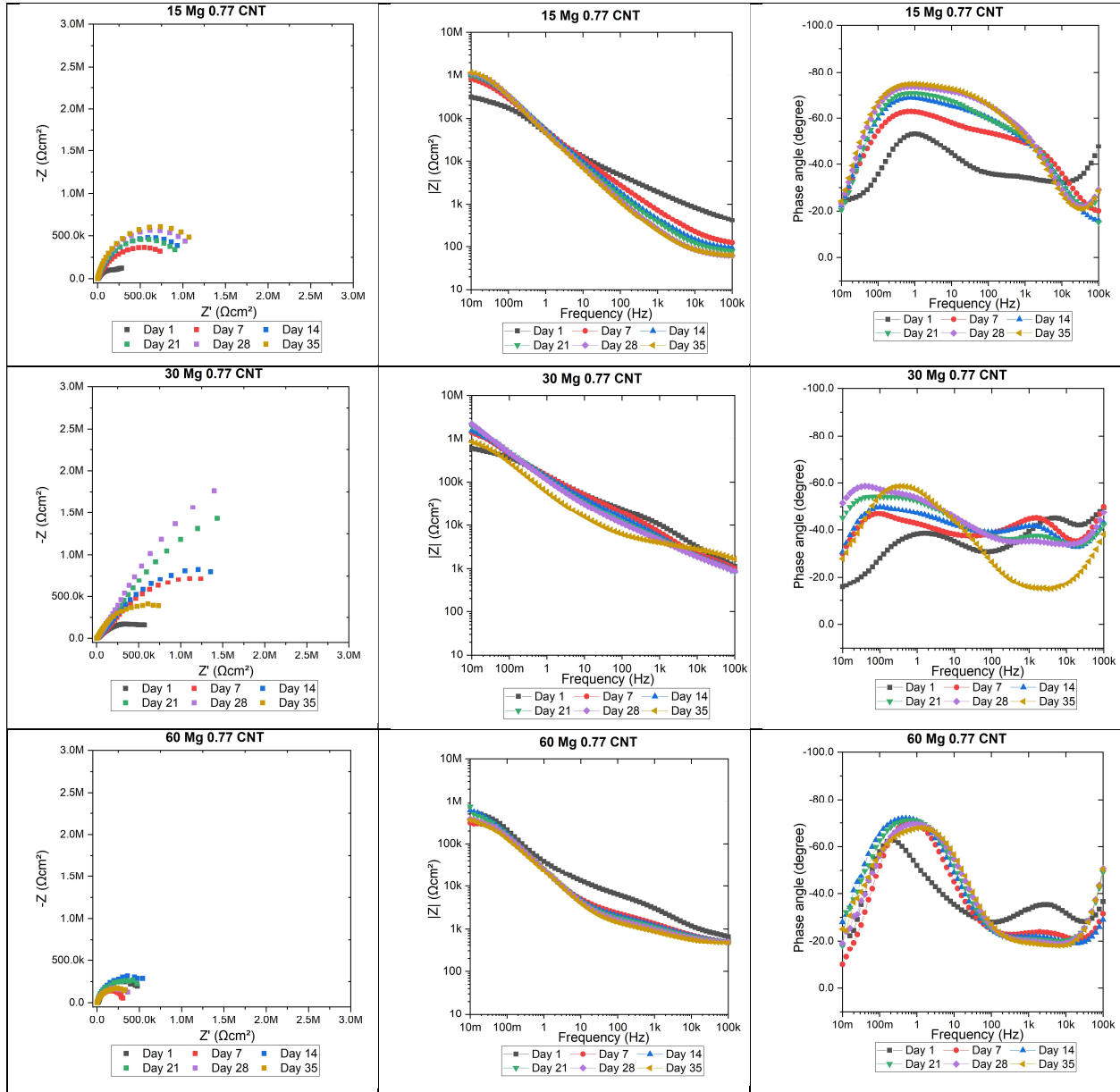
### **II.3.3. Influence of CNTs on the evolution and interfacial mechanisms**

For the 15% MgR particles, the addition of CNTs showed a defined mechanism over time. The total impedance magnitude was smaller in the presence of CNTs. Prior work has demonstrated how CNTs improve the electrical connectivity between active particles embedded within an epoxy matrix [xx]. CNTs also strengthen the barrier protection of active rich epoxy coatings. Previously, ZnR was used to protect the carbon steel matrix space and potential porous filling out with the small particles. The OCP showed a stable magnitude over time, as previously described. After the initiation stage, the OCP magnitude increased to more positive magnitudes and was located in the barrier region. Figure 10 shows the EIS signature when 0.77% CNT was added to the epoxy polymer. The mechanisms are proposed on the basis of the time constants that appeared at different frequencies.

The EIS characterization was based on three different stages. Under initial immersion conditions, water uptake and activation occurred. The MgR15 formulation showed three time constants. The first, at high frequencies, described the polymer properties. The phase angle describing the second time constant at medium frequencies related to the particle's properties in



the initiation-activation stage. The time constant was less clear than that in the previous composition without CNTs; the phase angle magnitude slightly changed over time on the following day. The interconnectivity between MgR particles increased in the presence of CNTs. Previously, smaller percentages of CNTs in ZnR epoxy coatings influenced the resistivity and



**Figure 10.** EIS Nyquist and Bode plots for Mg-rich primer-aluminum system with carbon nanotubes

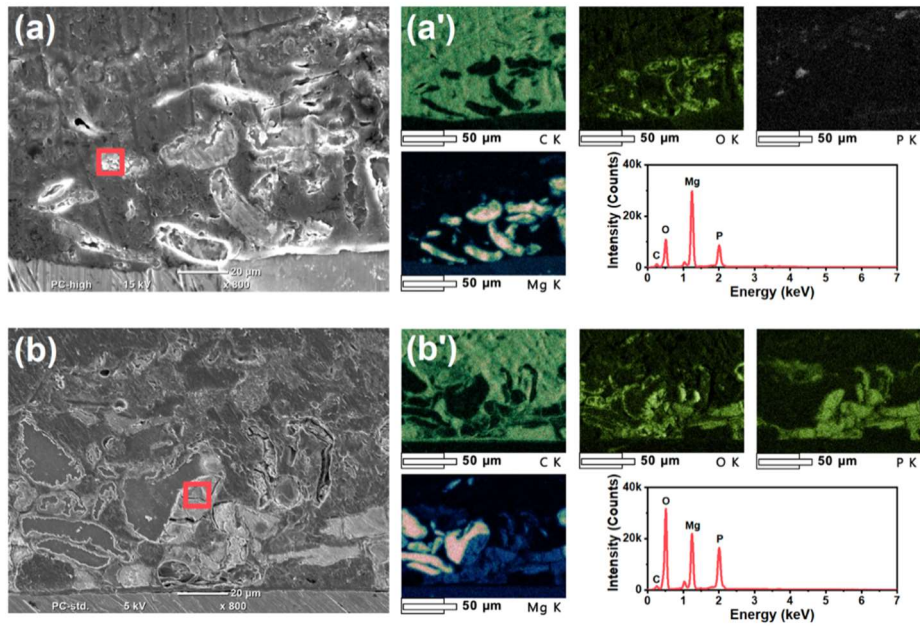
the surface activity of zinc particles, thus promoting charge transfer and mass transfer reactions at the particle-epoxy interface. The OCP was consistent with the stability of the activation stage in the initial stage, and the potential increase after immersion and entry into the barrier protection zone instead of the sacrificial mode (charge transfer). The rapid reaction and sites available for the electrochemical reaction with the MgR particles produced higher phase angle magnitudes at low frequencies: the magnitude started at 62 degrees and increased to almost 77 degrees. The mid frequency phase angle, indicating a time constant associated with the corrosion products, formed rapidly because of the activation or charge transfer mechanism. The CNT addition facilitated the interconnectivity between particles, the active area increased, the particles experienced an interfacial reaction, and the formation of corrosion products influenced the phase angle magnitude. This magnitude was greater than that with all previously tested concentrations of Mg without CNT addition. This finding was attributed to the higher total surface activity than that with the previously tested MgR formulations. The next stage after initiation is the active to passive transition, thus producing corrosion products at the particle interface. The final or steady state stage was marked by the water uptake electrolyte reaching all particles on the surface and the continuous charge transfer controlled process.

The addition of CNT to higher concentrations of MgR particles modified the evolution of the EIS signal in terms of interfacial stages and the mechanisms in the coating. At 30% Mg with CNT addition, two stages were identified. The initial stage consisted of water uptake with the activation of surface particles that reacted and formed charge transfer reaction products as the charge transfer reaction occurred. As shown in Figure 10, at the low-mid frequencies, the phase angle showed a maximum, owing to the charge transfer reaction and the influence of oxides or

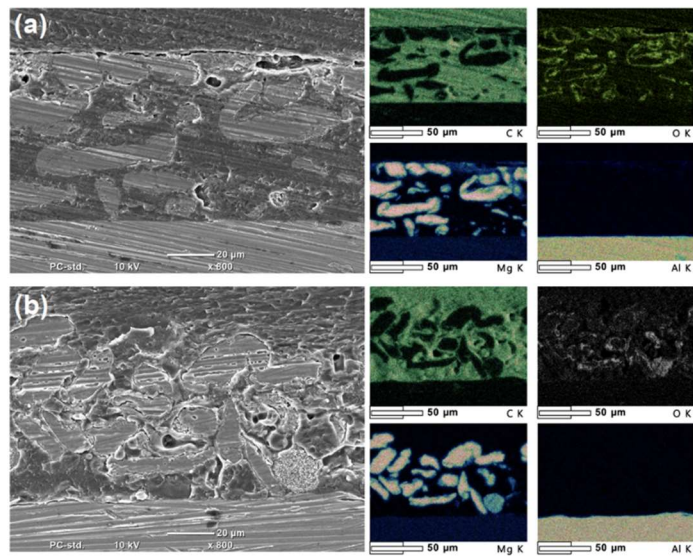
corrosion products, whereas at high frequencies, the influence of the polymer matrix contributed to the second time constant. After 7 days of exposure, the time constant at low medium frequencies increased in magnitude, and an additional time constant appeared at medium frequencies. This finding was attributed to the surface gained by the interconnectivity between the particles due to the presence of CNTs. More active surface was achieved by the electrolyte, owing to the particle-CNT-particle electrical connection. ZnR epoxy results in activation of more sites, owing to the interconnectivity between CNT and Zn particles at low percentages of CNT. In this work, the concentration of CNT helped to reveal more surface that had not reacted at the initial exposure time. The second stage was the activation-passivation, in which the electrolyte found new active surface.

The addition of CNT to the 60% Mg showed three stages and two time constants. The initial or activation stage was described by two time constants at high and low frequencies. The electrolyte was taken up by the polymeric matrix and wet the surfaces of the MgR particles, thus activating the surface after day 1. The second stage included the activation-passivation of MgR particles in the presence of CNTs from day 7 to day 35. Finally, the last stage was reached at 35 days, when the phase angle remained unchanged over time at low frequencies, and a stable phase angle magnitude was observed for the high frequencies.

The three different time constants shown in the phase angle are represented in Figure 13, with an equivalent circuit with three CPE and resistances from high frequency to low frequency describing the properties of the polymeric matrix, the particles, and the interfacial reactions at the particle/polymer interface.



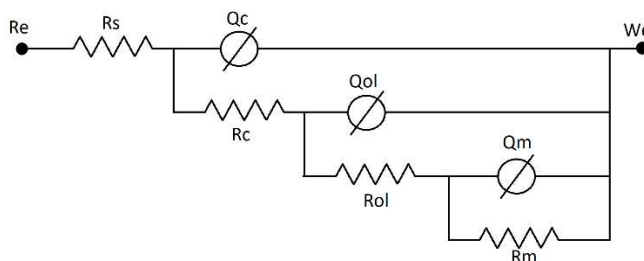
**Figure 11.** SEM and EDS of 15%Mg and 30%Mg coatings before immersion



**Figure 12.** SEM and EDS of a) 30%Mg 0%CNT and b) 30%Mg 0.77%CNT coatings after immersion

Mg Conc. (w%)	CNT Conc. (w%)	Immersed Time (Days)	POLYMER MATRIX			MAGNESIUM OXIDE			PARTICLE/POLYMER INTERFACE		
			Resistance ( $\Omega \text{ cm}^2$ )	Capacitance $S^*s^a$	Exponent	Resistance ( $\Omega \text{ cm}^2$ )	Capacitance $S^*s^a$	Exponent	Resistance ( $\Omega \text{ cm}^2$ )	Capacitance $S^*s^a$	Exponent
15	0	1	16330.0	7.22E-08	0.86	77260.0	3.62E-06	0.34	185600.0	1.65E-05	0.66
		7	14800.0	1.79E-07	0.77	114100.0	2.63E-06	0.51	464400.0	1.61E-05	0.76
		14	12260.0	3.49E-07	0.72	137500.0	2.59E-06	0.61	887700.0	1.30E-05	0.74
		21	7301.0	6.43E-07	0.68	125700.0	2.55E-06	0.70	897500.0	1.22E-05	0.70
		28	5462.0	9.92E-07	0.65	126600.0	3.03E-06	0.72	1033000.0	1.08E-05	0.67
		35	4973.0	1.18E-06	0.64	112700.0	3.25E-06	0.72	717700.0	1.41E-05	0.68
42	4003.0	2.42E-06	0.59	133600.0	4.09E-06	0.72	446400.0	1.36E-05	0.64		
30	0	1	107.4	3.45E-08	0.92	8056.0	7.65E-05	0.45	3581.0	3.68E-07	1.00
		7	541.2	3.78E-06	0.60	3081.0	1.64E-05	0.58	430200.0	9.37E-06	0.77
		14	982.1	4.35E-06	0.59	5866.0	1.19E-05	0.58	792700.0	7.36E-06	0.77
		21	1918.0	5.81E-06	0.56	14550.0	8.07E-06	0.58	1187000.0	5.77E-06	0.72
		28	2638.0	7.51E-06	0.54	29130.0	4.90E-06	0.57	1731000.0	4.48E-06	0.66
		35	2736.0	9.00E-06	0.53	86580.0	4.52E-06	0.53	2423000.0	2.28E-06	0.80
42	1235.0	1.00E-05	0.52	87850.0	3.40E-06	0.58	3551000.0	1.89E-06	0.80		
60	0	1	150.3	1.28E-06	0.69	31820.0	4.99E-05	0.49	93060.0	3.31E-03	1.00
		7	394.7	1.09E-05	0.60	2498.0	1.02E-05	0.68	258300.0	1.74E-05	0.78
		14	734.8	1.18E-05	0.65	4824.0	7.22E-06	0.77	865800.0	1.44E-05	0.83
		21	725.4	1.50E-05	0.66	7900.0	6.25E-06	0.77	1800000.0	9.14E-06	0.88
		28	491.2	1.59E-05	0.68	8635.0	6.32E-06	0.78	1335000.0	7.58E-06	0.88
		35	481.2	1.89E-05	0.69	7979.0	3.80E-06	0.87	1181000.0	5.81E-06	0.90
42	368.8	2.11E-05	0.71	6069.0	2.78E-06	0.93	740200.0	4.89E-06	0.91		
15	0.77	1	161.2	1.79E-05	0.75	2555.0	8.01E-06	0.80	138500.0	7.49E-06	0.84
		7	92.1	1.47E-05	0.79	1972.0	1.02E-05	0.83	170000.0	7.37E-06	0.85
		14	11.8	1.21E-06	0.79	287.0	1.83E-05	0.81	157700.0	1.46E-05	0.83
		21	9.2	8.95E-07	0.84	190.0	2.07E-05	0.84	185500.0	1.26E-05	0.84
		28	9.5	7.50E-07	0.84	149.1	2.00E-05	0.85	181300.0	1.47E-05	0.85
		35	10.1	9.30E-07	0.83	233.2	2.23E-05	0.85	218000.0	1.38E-05	0.86
42	10.0	1.18E-06	0.82	250.4	2.32E-05	0.85	219600.0	1.37E-05	0.86		
30	0.77	1	524.4	2.31E-08	0.87	3944.0	2.88E-05	0.35	69480.0	2.07E-05	0.78
		7	613.8	2.45E-09	1.00	4161.0	8.55E-06	0.45	547700.0	2.55E-05	0.60
		14	664.3	7.27E-07	0.62	1606.0	1.49E-05	0.65	206900.0	2.01E-05	0.70
		21	539	1.12E-06	0.61	1620.0	1.72E-05	0.66	176500.0	1.89E-05	0.72
		28	271.3	1.40E-06	0.62	1686.0	2.31E-05	0.72	153500.0	1.26E-05	0.80
		35	483.7	1.71E-06	0.57	2399.0	2.04E-05	0.71	158500.0	1.45E-05	0.77
42	262.2	1.27E-06	0.61	2230.0	2.50E-05	0.74	121200.0	1.04E-05	0.84		
60	0.77	1	1160	1.48E-05	0.57	4022.0	1.36E-05	0.90	79870.0	2.37E-05	1.00
		7	95.39	1.52E-06	0.66	283.5	1.46E-05	0.73	43660.0	4.78E-05	0.90
		14	91.79	1.68E-06	0.65	210.2	1.38E-05	0.75	104100.0	5.17E-05	0.87
		21	76.16	2.13E-08	1.00	179.2	1.59E-05	0.73	90590.0	5.22E-05	0.86
		28	71.98	2.31E-08	1.00	153.0	1.97E-05	0.73	56650.0	5.04E-05	0.86
		35	66.16	2.50E-08	1.00	141.7	3.53E-05	0.69	60950.0	4.52E-05	0.87
42	67.37	2.87E-08	0.99	140.5	3.76E-05	0.71	59660.0	4.73E-05	0.87		

**Table 5.** Values of equivalent circuit fitting.



**Figure 13.** Equivalent circuit

## CHAPTER III

### NANOCOMPOSITE EPOXY-RICH COATINGS

#### III.1. Introduction

Stainless steel (SS) is widely used in the industry due to its excellent corrosion resistance and price. However, these materials tend to suffer localized corrosion due to the breakdown of the passivation layer formed on the steel surface [79]. One of the most efficient methods for shielding SS from corrosion is applying organic coatings, which provide a protective barrier and prevent the diffusion of oxygen and water through the insulating layer [80]. Epoxy resins, among organic coatings, are the most used polymers in the protection of steel due to their excellent physical and chemical properties such as adhesion, chemical resistivity, mechanical and dielectric properties [81]. However, like all polymers, they are susceptible to corrosive species such as oxygen, aggressive ions, and water molecules at the metal/coating interface, reducing the coating adhesion and favoring corrosion of the metal underneath the film [82, 83]. Incorporating inorganic nanoparticles, however, can improve the barrier properties and protective performance of the epoxy coatings. Examples of the inorganic materials include silicon oxide ( $\text{SiO}_2$ ), titanium dioxide ( $\text{TiO}_2$ ), zinc oxide ( $\text{ZnO}$ ), cerium oxide ( $\text{CeO}_2$ ), zirconium oxide ( $\text{ZrO}_2$ ), among others, recognized for their physical and mechanical properties owing to their grain size and grain boundary volume [80, 84].

Individual oxides of Zr, Zn, and Ti are among the commonly used materials for corrosion-resistant coatings and present good performance. However, the use of single oxide exhibits some flaws due to pores and cracks in the coatings. Contrarily, a hybrid or multi oxides coating can

potentially combine the intrinsic properties of all the oxides, improving the adherence and enhancing the barrier to dissemination and preclusion of charge transport. The properties of the coatings can be tailored by controlling the concentrations of each oxide nanoparticle to overcome the limitations within a single oxide [85, 86].

This study proposes a novel and hybrid combination of TiO<sub>2</sub>, ZnO, and ZrO<sub>2</sub> nanoparticles at different ZrO<sub>2</sub> rich ratios using the ball milling technique and added to a commercial epoxy resin. For the first time, we present a systematic fundamental analysis of the different nanoparticles' ratios in the epoxy matrix to determine the efficacy in the corrosion protection properties on SS substrates.

## **III.2. Experimentation**

### **III.2.1. Materials**

Stainless Steel 430 BA rectangular plate substrates (20 mm x 10 mm x 1 mm) purchased from Prominox. The substrates were abraded with successive grades of SiC papers up to 1500 grade and sequentially cleaned with sodium hydroxide (NaOH, 98% purity), sulfuric acid (H<sub>2</sub>SO<sub>4</sub>), hydrochloric acid (HCl 37 wt%), extran solution, methanol (CH<sub>3</sub>OH), and deionized water, blow-dried at room temperature with compressed air. The cleaning solvents used and the oxides ZrO<sub>2</sub>, ZnO, and TiO<sub>2</sub> were supplied by Sigma- Aldrich Company (Toluca, Mexico).

### **III.2.2. Synthesis of the trimetallic oxide compounds**

The three different oxides were weighed and mixed at different enriched ZrO<sub>2</sub> proportions, forming six different compositions (Table 6) of the TMO. All the mixed TMO were annealed at 700°C for 2 h in a non-vacuum oven and mechanically milled at 300 rpm for 3 h. Finally, the TMO nanocomposites were sintered at 700°C for 2 h.

**Table 6.** Composition of trimetallic oxides (wt%)

TMO	ZrO <sub>2</sub>	TiO <sub>2</sub>	ZnO
A	90	5	5
B	80	10	10
C	65	25	10
D	50	40	10
E	40	50	10

### III.2.3. Preparation and deposition of the epoxy-TMO coatings

The Epoxy-TMO coatings were prepared using commercial epoxy resin mixed with the different Z2T compositions in a proportion, epoxy resin(99-x) and TMO (x) wt%, using magnetic stirring for 15 minutes. After that, the commercial hardener was added to the mixture to obtain a 60:40 wt% of epoxy-catalyst mixed by magnetic stirring for 3 minutes and sonicated in deionized water to release trapped air bubbles inside the coating. The resulting Epoxy-TMO coatings were deposited on the metallic substrates by drop-casting, and the procedures were repeated to obtain uniform coatings. The resulting coatings were dried at room temperature for 24 h.

### III.2.4. Characterization

The crystal structure of the synthesized TMO and was characterized by X-ray diffraction (XRD) with a copper K $\alpha$  radiation source ( $\lambda=1.5405$  a) at a scan rate of 0.04° min<sup>-1</sup> using a Bruker AXS D8 Advanced apparatus. The oxides were analyzed in the 2 $\theta$  range from 10° to 80°.



The morphology and composition of TMO were studied using TESCAN Vega3 SEM fitted with Bruker EDS. Raman analysis was performed using NT-MDT Ntegra spectra with a shift in the range of 300 to 3300  $\text{cm}^{-1}$ . The optical absorbance of the coated films was characterized using JASCO V-670 Spectrophotometer in the wavelength between 200 and 600 nm.

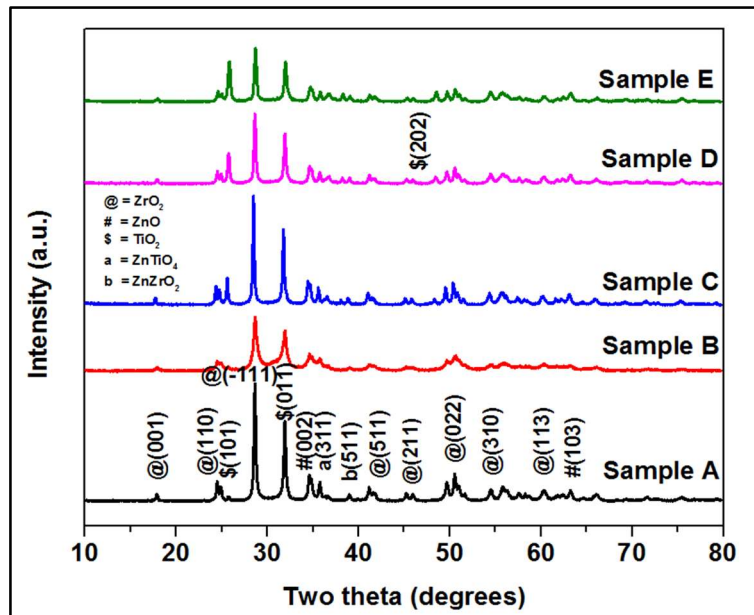
The electrochemical behavior of the non-scratched and scratched coatings was assessed in a 3.5 wt% NaCl solution at room temperature for various immersion times (i.e., from 1 to 28 days). The measurements were performed in a Potentiostat/Galvanostat (Gamry instrument REF600® potentiostat). A typical three-electrode was used: the coated SS substrate as the working electrode with an exposed area of 2.714  $\text{cm}^2$ , a saturated calomel electrode (SCE) as the reference, and a platinum grid wire as the counter electrode. The electrochemical techniques such as open circuit potential (EOCP), electrochemical impedance spectroscopy (EIS), and linear polarization resistance (LPR) were measured using a GAMRY REF600® potentiostat. EIS measurements were carried out at EOCP with a sinusoidal potential of 10 mV in amplitude. The frequency range was from 10<sup>-2</sup> to 10<sup>5</sup> Hz with 10 points per decade interval. The corrosion behavior of the commercial epoxy coating was also tested under the same conditions, providing a baseline for coating evaluation. Water contact angle was measured using Data physics (OCA 35, Germany) with 4  $\mu\text{L}$  distilled water.

### **III.3. Results and discussion**

#### **III.3.1. X-Ray Diffractogram analysis**

The synthesized Z2T nanocomposites characterized by XRD (Figure 14) shows characteristic  $2\theta$  peaks values at  $\sim 16.7^\circ$ ,  $24.3^\circ$ ,  $43^\circ$  for the  $\text{ZrO}_2$  monoclinic, with the prominent

peak at  $2\theta = 28.6^\circ$  corresponding to the (-111) plane (ICDD file no. 00-065-0728) [87]. It can be observed that increasing the wt% of tetragonal anatase-TiO<sub>2</sub> (ICDD file no. 01-070-2556) decreases the intensity of ZrO<sub>2</sub> [88]. The observed peak at  $2\theta = 34.4^\circ$  corresponding to the (002) plane suggests the presence of hexagonal ZnO (ICDD file no. 01-082-9744) [89]. The observed prominent peak at  $2\theta \sim 36.3^\circ$  may be attributed to (311) plane corresponding to the presence of tetragonal ZnTiO<sub>4</sub> (ICDD file no. 00-038-0500) [90]. It is also observed a small peak at  $2\theta \sim 40^\circ$  corresponding to the plane (511) of the ZnZrO<sub>2</sub>.



**Figure 14.** XRD of the synthesized TMO ZrO<sub>2</sub>: ZnO: TiO<sub>2</sub> by ball milling

The average crystallite size (Table 7) for each oxide was calculated with the Debye-Scherrer equation inserting the diffraction angle and peak full line width at half maximum (FWHM):

$$D = \frac{0.94\lambda}{\beta \cos\theta}$$

D is the crystallite's average size,  $\lambda$  is the wavelength of the X-ray radiation, B is the peak FWHM in radian, and  $\theta$  is the diffraction peak position.

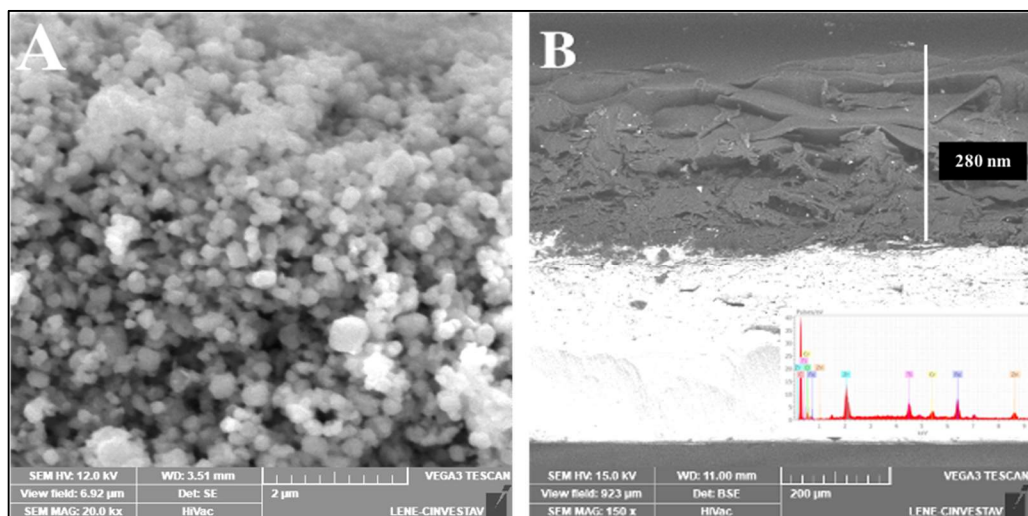
**Table 7.** Average crystallize size of the TMO oxides

TMO	ZrO <sub>2</sub> (nm)	TiO <sub>2</sub> (nm)	ZnO (nm)	ZnTiO <sub>4</sub>	ZnZrO <sub>2</sub>
A	12.22	20.97	26.50	37.50	35.05
B	12.50	15.47	19.14	35.02	34.36
C	18.37	17.51	18.61	45.36	34.50
D	26.67	15.94	16.87	43.99	31.46
E	26.59	16.53	17.04	40.68	34.56

The ZrO<sub>2</sub> crystallite sizes varied between 12 and 27 nm, improving the wt% of TiO<sub>2</sub>, although with a marginal decrease in sample E. The crystallite sizes reduced and remained almost constant afterward for TiO<sub>2</sub> but gradually reduced for ZnO.

### III.3.2. Morphological characterization of trimetallic oxides

The SEM micrograph of the Z2T TMO shows agglomerations of the nanoparticles with a random uniform distribution of the constituent elements (Figure 15A). The SEM micrograph shows the distribution of grains of trimetallic oxide in the range of 100 to 400 nm by EVA software. The average thickness for all the epoxy samples measured from the cross-section (Figure 15B) is around 280 nm.



**Figure 15.** A) SEM micrographs of TMO ( $ZrO_2/TiO_2/ZnO$ ), B) Cross-section SEM images of epoxy-TMO coating in a stainless steel substrate.

The elemental composition of the depositions (Table 8) showed a higher constituent of Zr in all cases (except in sample E); Fe and Cr belong to the substrate, while the carbon content (above 80%) is obtained from the epoxy material.

**Table 8.** Elemental compositional for cross-section image of epoxy film with different trimetallic oxide compositions

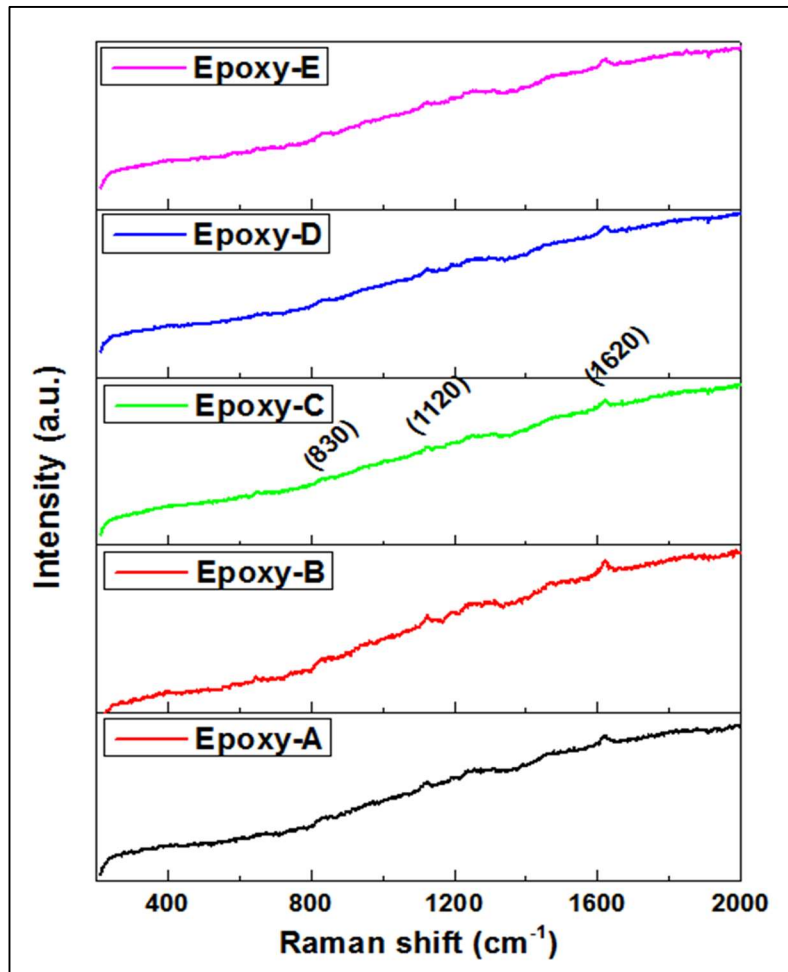
Samples	C (%)	O (%)	Zr (%)	Zn (%)	Titanium (%)	Cr (%)	Fe (%)
A	83.82	8.97	2.85	0.69	0.59	0.76	2.32
B	86.42	5.19	3.22	0.90	1.24	0.92	2.11
C	86.91	5.91	2.15	1.04	1.45	0.63	1.91
D	82.68	6.85	2.23	0.47	1.33	2.24	4.20
E	82.88	7.38	1.54	0.53	1.61	2.93	3.13

### **III.3.3. Raman analysis**

In Figure 16 it is presented the Raman analysis of the epoxy coatings with the TMO oxides to determine if the phases characterized by XRD were presented in the coatings where it is reported that composites for ZnO wurtzite and monoclinic ZrO<sub>2</sub> maintain their phases after annealing at 700°C [91]. The observed peaks at 1120 and 1620 cm<sup>-1</sup> corresponded to the benzene ring quadrant stretching characteristics of the epoxy ring vibration, the signal at 830 cm<sup>-1</sup> could also be related to the vibrations of the entire epoxy ring (i.e., characteristic of the CH<sub>2</sub> Epoxy asymmetric, and vibration C-H groups of the epoxy ring) [92]. The lacking peaks of TMO oxides (1 wt%) may be due to their relative amount, which is not enough to exhibit significant peaks in the Raman modes corresponding to the present oxides.

### **III.3.4. Optical analysis of epoxy-rich coating**

The epoxy systems have significant chemical and mechanical properties. They possess aromatic groups with strong absorption in the UV range at 300 nm, making the epoxy structures susceptible to photodegradation. UV light forms free radicals on the surface of the polymer and is highly active in attacking the polymer structures. Other environmental factors, including humidity, oxygen, temperature, and pollutants, can decrease the lifetime of the polymer. Thus, added inorganic nanoparticles such as ZnO and TiO<sub>2</sub> scatter the light and have broad absorptions in the UV range, and almost do not have absorptions in the visible range [93]. The absorbance and transmittance plots for the coatings (Figure 17) showed two characteristic absorption peaks of the epoxy resin at ~280 and ~350 nm.



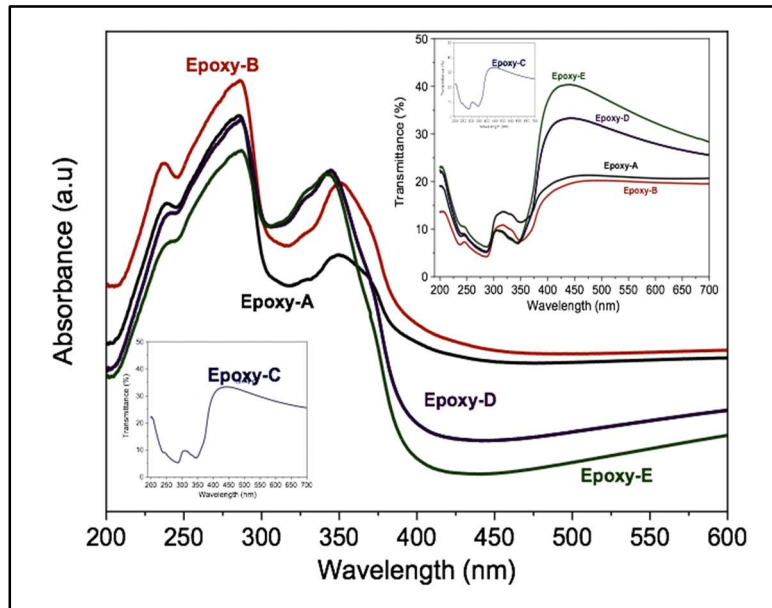
**Figure 16.** Raman of the epoxy- TMO coatings at different ratios of ZrO<sub>2</sub>/ TiO<sub>2</sub>/ ZnO: Epoxy-A (90/5/5), Epoxy-B (80/10/10), Epoxy-C (65/25/10), Epoxy-D (50/40/10), Epoxy-E (40/50/10)

From the transmittance plot, all the coatings presented low transmittance %, showing the coatings' capacity to absorb light. Except for the epoxy-A coating, all the coatings present a transmittance % close to each other.

Incorporating TiO<sub>2</sub> nanoparticles within the epoxy coating tends to broaden the absorption region of the epoxy and enhance the absorption intensity at around 250 nm within the TiO<sub>2</sub> absorption range. Thus, the UV range is enhanced by incorporating this oxide, observed from

(Figure 17) for the deposited coatings [94]. The enhancement may be due to TiO<sub>2</sub>, which has a wide bandgap  $\sim 3.2$  eV and tends to absorb the shorter wavelength with high energy to excite its electron below 400 nm where it does not have a specific peak within this region. The absorption range of nano ZnO reported between 360- 230 nm can also block the UV radiation in organic coatings [95] and observed at  $\sim 246$  nm (Figure 17).

Xu et al. [96] reported that TiO<sub>2</sub>/ZnO composites presented strong photo-absorption than pure ZnO and TiO<sub>2</sub>. The absorption edge of TiO<sub>2</sub>/ZnO showed a redshift to the visible spectrum range ascribed to better scattering of the induced electron-hole pairs in the porous architecture as well as the mixture effect of the bandgap of the composite semiconductor improving the photoelectric effect of the composite films and further enhance their photocathodic properties of the stainless-steel substrate.



**Figure 17.** UV absorbance of the synthesized coatings epoxy- TMO coatings: Epoxy-A (90/5/5), Epoxy-B (80/10/10), Epoxy- C (65/25/10), Epoxy-D (50/40/10), Epoxy-E (40/50/10).

ZrO<sub>2</sub> presents excellent chemical and physical properties, with a wide bandgap larger than 5 eV, is crucial luminescent material. Its good optical transparency makes it a potential candidate for photocatalytic applications due to its high surface area and many oxygen vacancies. The monoclinic phase appears more stable at room temperature, depending on the different synthesis parameters with reported absorption signal ~204 nm [97]. In the Epoxy-TMO, the signal is not observed within these ranges. The signal corresponding to an interaction between ZnO and ZrO<sub>2</sub> is observed ~246 nm, decreasing with a reducing ZrO<sub>2</sub> ratio in the coatings. Sathyaseelan et al. [98] reported absorption peaks at 215 and 217 nm for synthesized and calcined samples of ZrO<sub>2</sub> due to the Zr<sup>4+</sup> ions d transition. The nanoparticles also showed a weak absorption band at 310 nm due to mid-gap trap sides, such as surface defects and oxygen vacancies. The surface modification results in a sharp increase in absorption by the ZrO<sub>2</sub> within the visible region.

### **III.3.5. Contact Angle measurements**

Water contact angle measurements (CA) were carried out for the epoxy-TMO coatings to investigate the coated surfaces' wettability state and determine the effects of the different oxides on the coated systems (Table 9). For the epoxy sample, it was not possible to determine a contact angle, and for the epoxy coatings with the nanoparticles, there is a difference in the CA. However, the trend showed no significant variation of the contact angle with the decrease of ZrO<sub>2</sub>. All the epoxy coatings present hydrophilic characteristics close to 90° except for the coating epoxy-D coating, which presented a CA of ~73.8° compared to the other coatings, exhibiting more hydrophilic characteristics. In comparison, the reported values of CA for ZrO<sub>2</sub> and ZnO are 67° and 75° respectively [99].

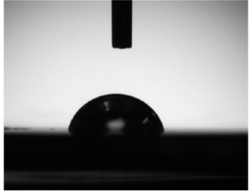

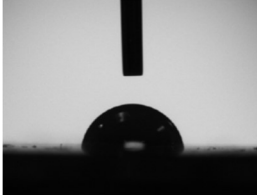
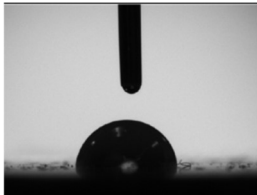
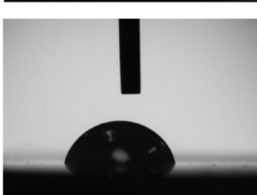
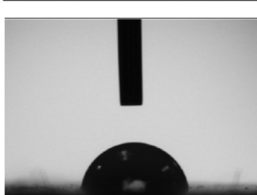


For these Epoxy- TMO coatings, there are two things related to reducing the water contact angle: the first is the characteristics and properties of the trimetallic nanoparticles. The second is the surface roughness and porosity of the coating. ZrO<sub>2</sub> has the property to increase the contact angle, reducing the wettability of the material [100]. TiO<sub>2</sub> shows a self-cleaning action related to its photocatalytic activity. The relationship between TiO<sub>2</sub> and hydrophilicity is that the water molecules will be chemisorbed on the TiO<sub>2</sub> surface. These water molecules will further absorb water by physisorption (Van der Waals forces or hydrogen bonds). The physisorbed water molecules act as a barrier to prevent close contact between surface and pollutants. The combination of TiO<sub>2</sub> with ZnO improves the hydrophilicity due to the formation of surface oxygen vacancies [101]. Sanu et al. also explained that reducing the contact angle can also reduce Ti<sup>+4</sup> cations to Ti<sup>+3</sup> state and oxidation of O<sub>2</sub><sup>-</sup> anions expelling some oxygen atoms. When the surface is exposed to moisture, the OH molecules are physisorbed to the vacancy sites, and the adsorbed OH groups on the surface can convert the surface into a hydrophilic one by creating a sheet of chemisorbed H<sub>2</sub>O through Van der Waals forces that block the close contact between the surface and adsorbed contaminants. Thus, the dirt absorbed on the film's surface can be quickly detached using water spread on the surface, showing a self-cleaning effect [102].

### **III.3.6. Electrochemical characterization**

EIS spectra illustrate the interfacial characterization with time-based on the coating composition. Figure 18a-c displays three EIS signatures (Nyquist, Bode, and phase angle) for the Epoxy and the Epoxy with TMO compositions following 21 days of 3.5% NaCl exposure. The representing values of this interface display high resistance after 21 days of exposure. The classic water uptake process occurring in a polymeric matrix coating prevails during the initial times,

**Table 9.** Contact angle measurements of epoxy-TMO coatings

Sample	Thickness ( $\mu\text{m}$ )	Contact angle	Drop image
Epoxy	340	NA	
Epoxy-A	270.8	$85.7\pm 0.4$	
Epoxy-B	253.9	$81.2\pm 0.3$	
Epoxy-C	271.2	$84.6\pm 0.4$	
Epoxy-D	292.5	$73.8\pm 0.3$	
Epoxy-E	302.6	$81.9\pm 0.3$	

achieving resistances are in the order of  $10^6$ - $10^{11} \Omega \text{ cm}^2$ . The Epoxy coating showed a typical water uptake behavior with time. The semicircle or loop shape by the complex representation resembles the epoxy evolution in a typical charge transfer and capacitance due to the water uptake within the matrix. The coating has a finite impedance magnitude marked by the loop magnitude ( $\sim 80 \times 10^8 \text{ ohm-cm}^2$ ). Epoxy-A illustrates a finite impedance magnitude with a high magnitude. The complex representation shows capacitive characteristic mechanisms due to the electrolyte uptake, and 95/5/5 confer barrier properties to the polymer matrix. The addition of  $\text{TiO}_2/\text{ZrO}_2$  permits the formation of a physical barrier; previously,  $\text{TiO}_2$  has been used in pigments to block electrolyte transport. The  $\text{ZrO}_2$  also helps the reduction of ionic species reaching the bulk of the polymer. The particles are distributed along with the polymeric matrix.

The addition of a higher percentage of  $\text{TiO}_2$  gives similar properties as the previous epoxy composition. Epoxy B formulation denotes controlled water uptake with a capacitive-like behavior due to the higher impedance similar to Epoxy A with the phase angle in both cases (Epoxy A and B) appearing identical along with the frequency range. Epoxy C contains no higher concentration of  $\text{TiO}_2$  and  $\text{ZnO}$  but a decrease in the  $\text{ZrO}_2$  concentration. The results following 21 days present a change in the transport mechanism and an increase of impedance magnitude. The Nyquist (or complex) plot presents a diffusion signature characteristic of the mass transport control process at low frequencies. The higher concentration of  $\text{TiO}_2$  influences the particle distribution within the matrix and the transport mechanisms. The particles are integrated with the polymeric matrix making an additional barrier layer influencing the electrolyte transport. Mass transport is characteristic of the complex signature and also the phase angle format at the lowest frequencies. It is essential to notice that epoxy- D coating with a proportion of 50/40/10 ( $\text{ZrO}_2/\text{TiO}_2/\text{ZnO}$ ) is the one with the highest resistance reaching values

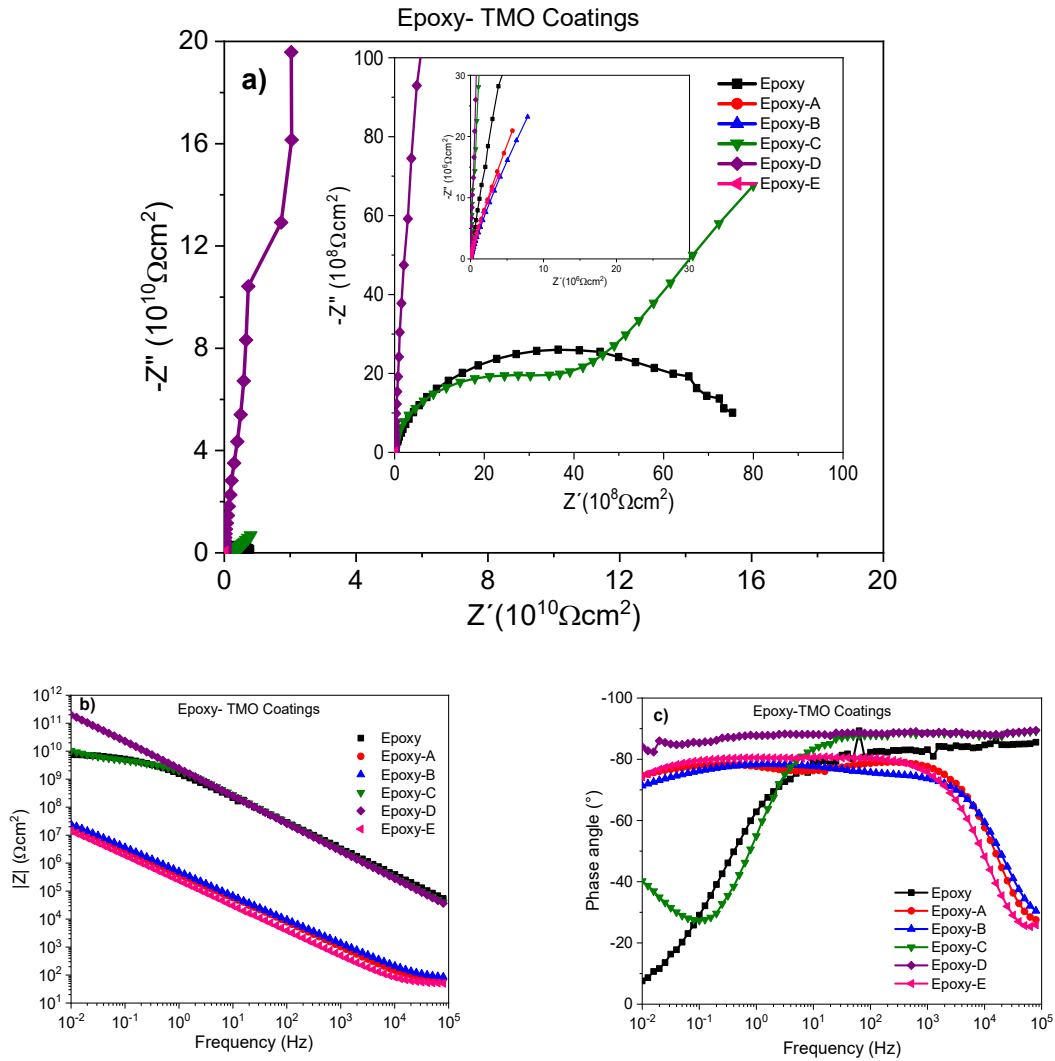
close to  $10^{12} \Omega\text{cm}^2$  with an ideal capacitance behavior with an infinite real impedance. This latter suggests a dielectric barrier blocking any water uptake and electrolyte draining within the coating during the exposure time. The highest percentage of  $\text{TiO}_2$  influences the transport mechanisms within the polymeric coating layer, the formation of an ideal capacitor considers the distribution of particles favoring the physical barrier within the polymeric matrix. The semiconductor properties due to  $\text{TiO}_2$  presence illustrate the blocking of the ionic species or any electrolyte within the polymeric matrix.

The  $\text{TiO}_2$  has been used for the filling of pores in polymeric materials.  $\text{TiO}_2$  has been used as pigment for several coatings; the pigment has been used for corrosion protection based on the physical barrier effect.

The epoxy-TMO coatings presented good resistance behavior by assuming physical barrier protection due to the properties of  $\text{ZrO}_2$  that could present isolator and conductive behavior, and that with the interactions of  $\text{TiO}_2$  and  $\text{ZnO}$ , the coating presents an additional barrier by using the  $\text{TiO}_2$  particles as fillers and blockers. The particle distribution suggests a random distribution within the polymer matrix and also at the coating surface. The contact angle is clear evidence of the influence of the distribution; the  $\text{TiO}_2$  is present at the outmost surface lowering the contact angle. The contact angle and resistance properties decrease with  $\text{TiO}_2$  increase, wetting the surface and not taking into the matrix.

Epoxy D shows a phase angle magnitude close to 90 degrees along with the frequency range and total impedance magnitude reached  $1e10^{11} \text{ ohm.cm}^2$  following 21 days of exposure. The transition of interfacial mechanisms was evident with the increase of  $\text{TiO}_2$  particles while  $\text{ZrO}_2$  decreases and  $\text{ZnO}$  remains constant. The 90/5/5 ( $\text{ZrO}_2/\text{TiO}_2/\text{ZnO}$ ) ratio showed water uptake with the coating, displaying a capacitance and finite charge transfer process. The increase of  $\text{TiO}_2$

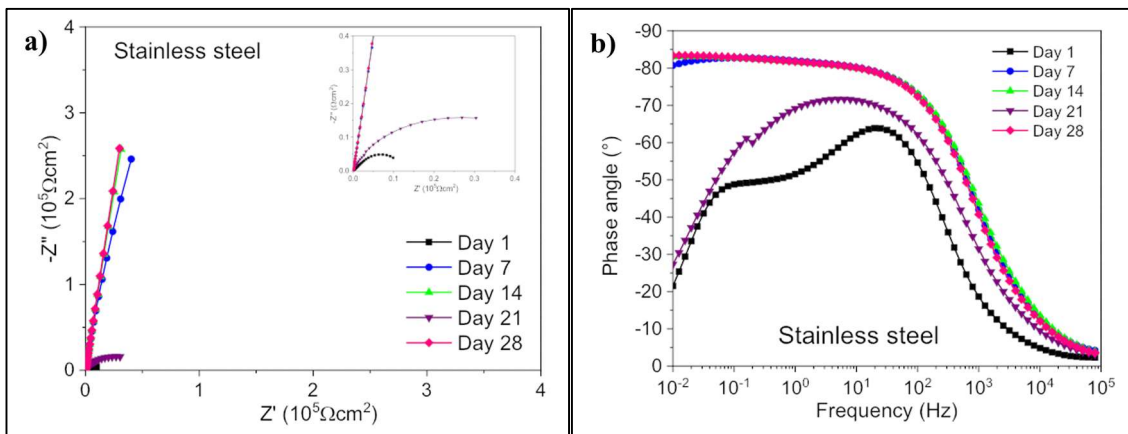
in the oxide composition (65/25/10- ZrO<sub>2</sub>/TiO<sub>2</sub>/ZnO) turns the mechanism more diffusion-controlled. This latter is due to a barrier layer influenced by the TiO<sub>2</sub> particles and the lower conductivity by decreasing ZrO<sub>2</sub>. Finally, the highest concentration of TiO<sub>2</sub> (50/40/10- ZrO<sub>2</sub>/TiO<sub>2</sub>/ZnO) produces an ideal capacitance behavior. The particles might form a dielectric layer with no passage of electrolyte, producing an ideal capacitor. Figure 18a-c displays the

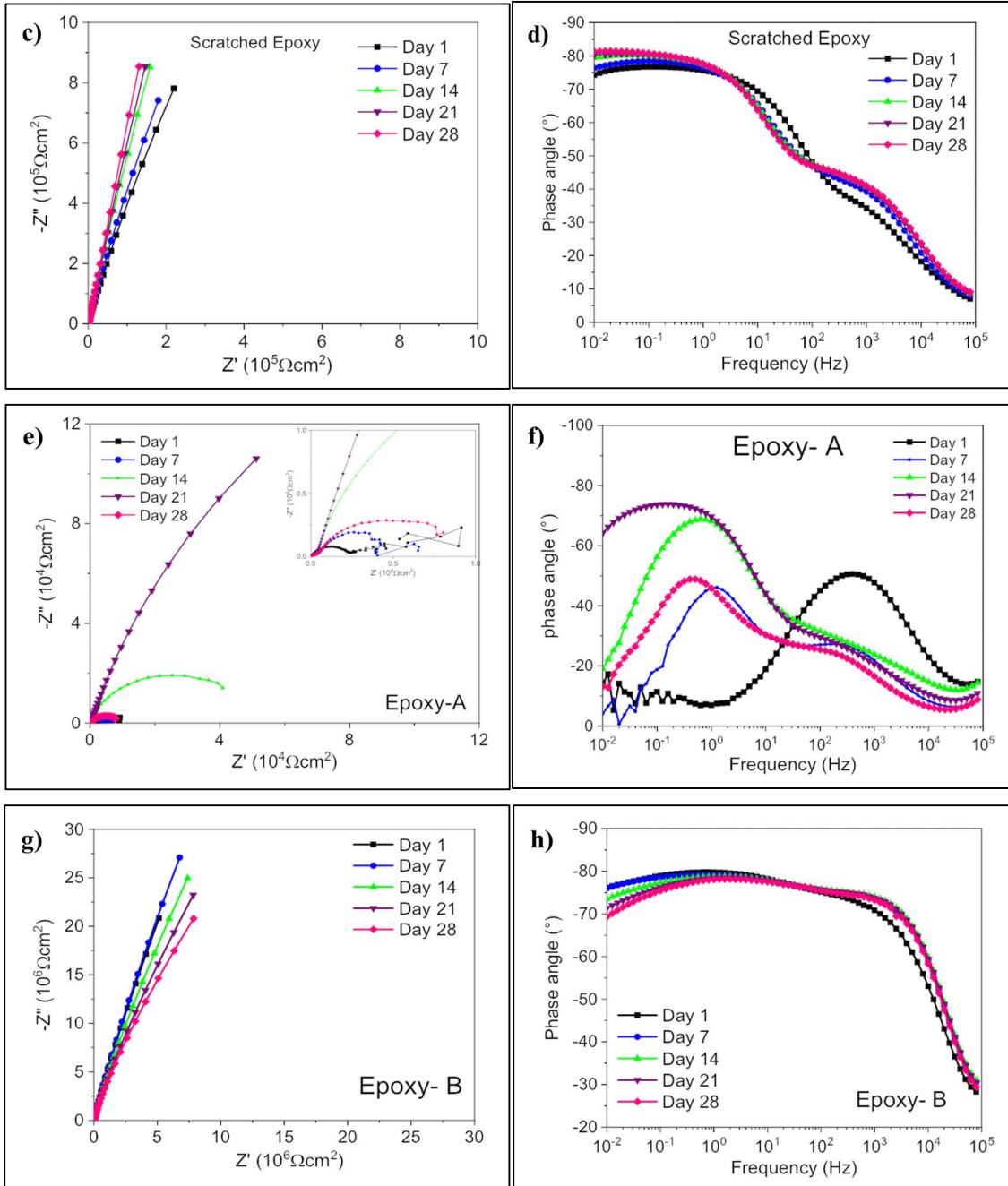


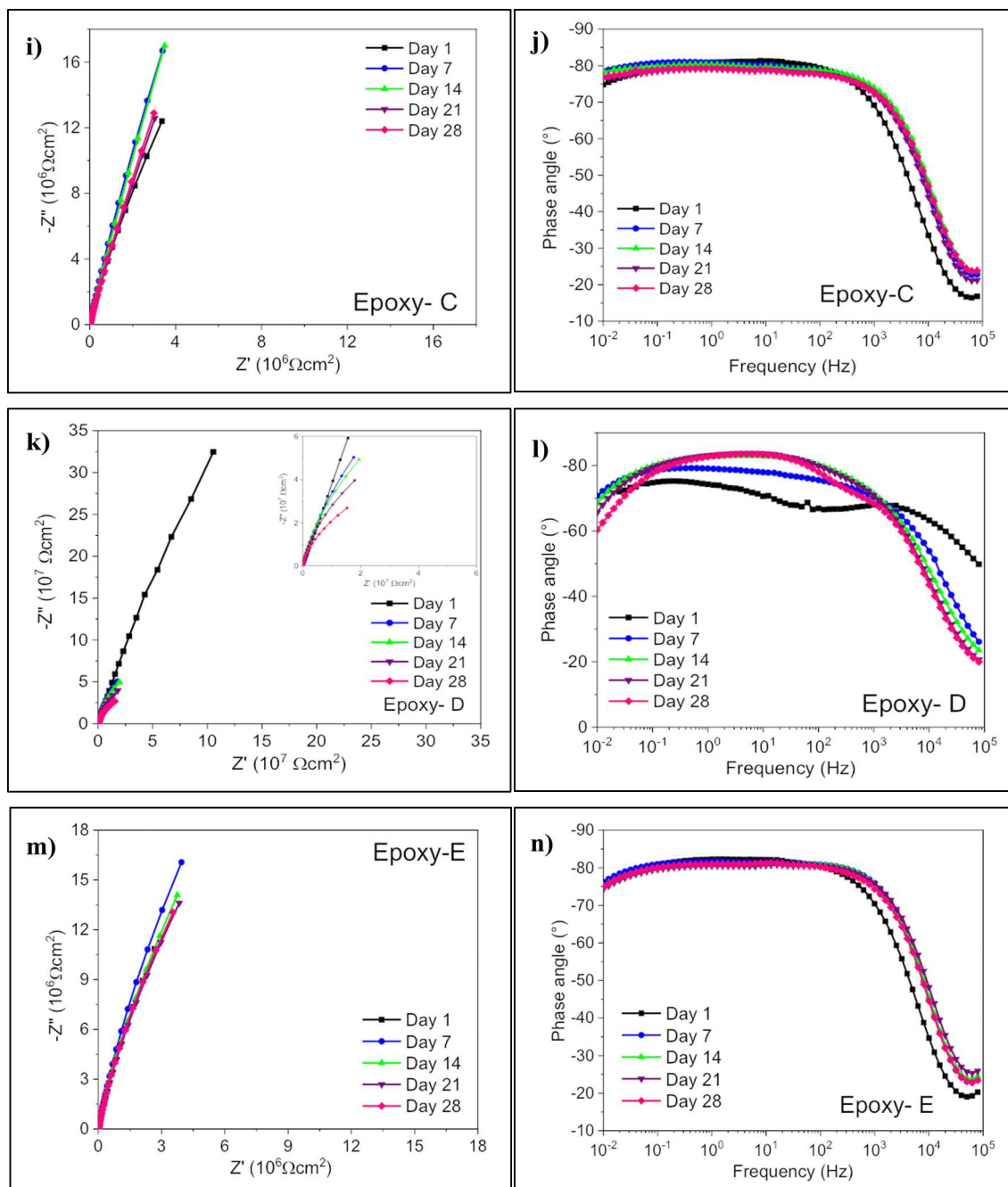
**Figure 18 .** Nyquist (a), Bode (b) and phase angle (c) of the epoxy and epoxy-TMO coatings at Day 21

damage or performance evolution of the coatings with the time-based distribution of the oxides within the coating. The physical barrier mechanism could be affected by removing the coating by mechanical load and presenting (Figure 19a-n) the same concentrations of coatings layers scratched and tested for 28 days exposed to NaCl solution. EIS signatures are presented in the three formats. Also, the substrate and the substrate with the Epoxy scratched condition is considered as the control system.

Stainless steel shows two-time constants due to the natural layer formed at an initial stage and evolving to have a capacitance-like behavior with an active-passive surface influenced by the corrosive environment. Following 28 days, the passive layer formed prevails for the metallic substrate. The mechanical scratch on the epoxy layer revealed the interfacial mechanisms when exposed to the corrosive electrolyte. The EIS signature displays the same trend as in the stainless-steel sample. At the initial stage, the complex diagram shows capacitance-like behavior, and two-time constants appear due to the natural layer formed and exposed to the corrosive environment.







**Figure 19.** Nyquist and phase diagrams of the stainless steel (a-b), and the scratched coatings epoxy (c-d) and epoxy-TMO coatings at different ratios of  $\text{ZrO}_2/\text{TiO}_2/\text{ZnO}$ : Epoxy-A (90/5/5) (e-f), Epoxy-B (80/10/10) (g-h), Epoxy-C (65/25/10) (i-j), Epoxy-D (50/40/10) (k-l), Epoxy-E (40/50/10) (m-n)



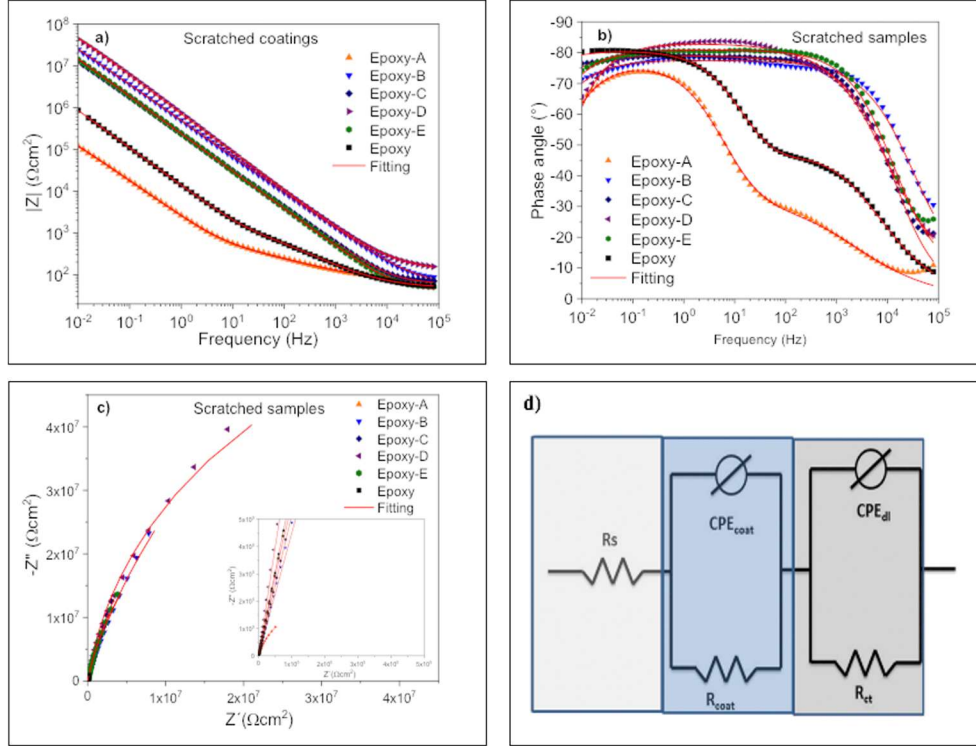
Epoxy-A coating with the highest content of ZrO<sub>2</sub> (Figure 19e-f) presented a decrease in the resistance in almost one order of magnitude compared to the scratched epoxy polymer. This behavior could probably be to the disbondment of the polymer close to the scratch on the polymer. The formation of one and later two-time constants with low phase angle magnitude is attributed to the polymer matrix's reaction. The resistive properties of the trimetallic oxides are also contributing to the evolution within the polymer matrix from day 7 to day 14 at mid to high frequencies. The disbondment can also be attributed to a lack of substrate interface adherence due to the particle distribution.

Epoxy B and C sustain a similar signature for the complex and phase angle representation. The minor difference is related to the mid frequencies' response. Epoxy B shows a lower phase angle magnitude comparing with Epoxy C. The particle distribution, coupled with decreased ZrO<sub>2</sub> content, and high TiO<sub>2</sub> in the polymer matrix, helped in the barrier effect in the matrix (mid frequencies) and the increased impedance magnitude of 106-107 Ωcm<sup>2</sup> overall.

Epoxy coating- D (Figure 19k-l) showed the highest resistance with an increase of two orders of magnitude than the scratched epoxy coating. As previously mentioned, this coating has a TMO oxide proportion of 50/40/10 (ZrO<sub>2</sub>/TiO<sub>2</sub>/ZnO) and showing an expected coating behavior that in contact with the aggressive environment, the resistance decreased to ~7x10<sup>7</sup> Ωcm<sup>2</sup> on day 14. However, this resistance is the highest compared to the other coatings; this latter agrees with the non-scratching condition with the Epoxy D showing good barrier protection due to the particles present in the polymer matrix.

Quantitative analysis is proposed using equivalent circuits on day 21. The Bode, phase diagram, and Nyquist are shown in Figure 20a-c, and the corresponding equivalent circuit is presented in Figure 20d. The obtained data for the simulation is presented in Table 10, using the

proposed equivalent analog circuit to characterize the interfacial processes occurring for each Epoxy system [103].



**Figure 20.** Bode (a), phase angle (b), Nyquist (c) and equivalent circuit (d) of the epoxy and epoxy-TMO scratched coatings at Day 21

**Table 10.** EIS fitting analysis of the scratched epoxy and epoxy-TMO coatings

Samples	$R_s$ ( $\Omega\text{cm}^2$ )	$R_{\text{coat}}$ ( $\Omega\text{cm}^2$ )	$Y_{0\text{coat}}$ ( $\text{S}^*\text{s}^\eta$ )	$\eta$	$Y_{0\text{dl}}$ ( $\text{S}^*\text{s}^\eta$ )	$\eta$	$R_{\text{et}}$ ( $\Omega\text{cm}^2$ )	$\chi^2$
Epoxy	48.12	731.9	$35.80 \times 10^{-6}$	0.613	$13.89 \times 10^{-6}$	0.898	$33.46 \times 10^6$	$77.05 \times 10^{-6}$
A	69.39	366.9	$167.2 \times 10^{-6}$	0.505	$83.47 \times 10^{-6}$	0.861	$478.7 \times 10^3$	$975.2 \times 10^{-6}$
B	56.59	$11.74 \times 10^3$	$145.1 \times 10^{-6}$	0.456	$411.9 \times 10^{-9}$	0.869	$155 \times 10^6$	$1.586 \times 10^{-3}$
C	60.38	$136.6 \times 10^3$	$25.1 \times 10^{-6}$	0.690	$866.5 \times 10^{-9}$	0.889	$173.8 \times 10^6$	$1.688 \times 10^{-3}$
D	93.74	$41.42 \times 10^6$	$168.9 \times 10^{-6}$	0.356	$253.5 \times 10^{-9}$	0.924	$127.2 \times 10^6$	$683 \times 10^{-6}$
E	5.366	$1.372 \times 10^3$	$8.065 \times 10^{-3}$	0.901	$802.7 \times 10^{-9}$	0.899	$102.2 \times 10^6$	$1.827 \times 10^{-3}$

The coatings presented an equivalent circuit in series, as shown in Figure 20d.  $R_s$  represents the solution resistance,  $R_{coat}$  is the resistance of the coating at high and middle frequencies, and  $R_{ct}$  is the resistance to the charge transfer related to the substrate coating interface at low frequencies. A constant phase element (CPE) was used to account for the surface conditions of the substrate. The CPE (ZCPE) is defined by  $Z_{CPE} = (1/Y)/(j\omega)^\eta$ , where  $\omega$  is frequency,  $Y$  is pseudo-capacitance, and  $\eta$  is associated with the system homogeneity specifying the CPE power, with parameters between -1 and 1 where  $\eta$  is between 0 and 1, the element has a CPE of the resistor-capacitor behavior [104, 105]. Table 10 shows the solution resistance of the coatings was less than  $100 \Omega\text{cm}^2$  and the resistance to charge transfer increased in the order of  $106 \Omega\text{cm}^2$  with increased  $\text{TiO}_2$  to  $\text{ZrO}_2$  and  $\text{ZnO}$  ratio, and increasing the capacitive behavior, which is higher considering the conditions of the coatings and the time immersed in the aggressive environment.

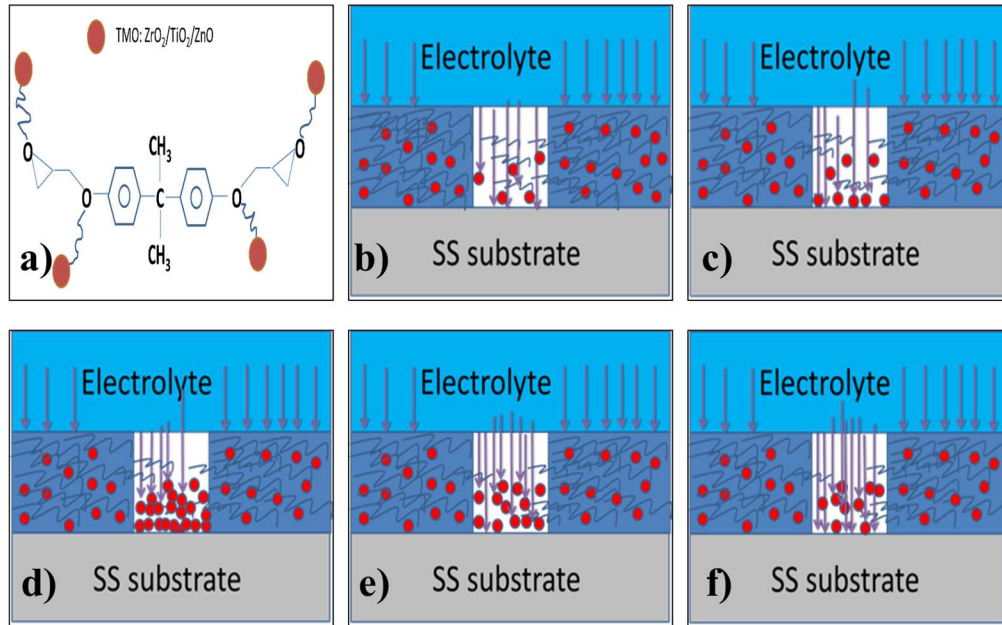
As mentioned before, the presence of the nanoparticles increases the corrosion resistance in the polymer coating. The epoxy- $\text{TiO}_2$  obtained by adding the  $\text{TiO}_2$  nanoparticles to modify the network structure of the polymeric epoxy matrix using the embedded nanoparticles contributed to reorganizing the polymeric matrix by physical interactions due to Van der Waals force that helps in closing up the pores of the epoxy matrix. Hence, forcing the penetrated electrolyte to travel a longer distance reaches the substrate surface and leads to the corrosion reaction initiation [106]. Kumar et al. reported that with higher loading ratio of  $\text{TiO}_2$  could affect its dispersion state and led to larger clusters, altering the contact among the nanoparticles and the epoxy matrix and narrowing their interaction are essential for interfacial adhesion [107]. The application of  $\text{ZnO}$  to these TMO oxides helped reduce the formation of the clusters and increased the film's corrosion resistance and barrier properties [108].

Incorporating the TMO on the Epoxy helped increase the corrosion resistance of the coating because the conformation of the three oxides forms a synergy between them and the organic coating. This type of corrosion resistance was observed for coatings with two oxides such as TiO<sub>2</sub>- SiO<sub>2</sub>. The constant phase elements show capacitive behavior and adding these elements indicated the entry of ions and corrosive solution to the lower layers of the coating. The observation was due to the presence of cracks and holes in the coatings, the lower barrier layers counteract the passage of the corrosive material to the substrate, increasing the corrosion resistance [109]. This kind of observation was also observed for epoxy resin with nanoparticles SiO<sub>2</sub>- ZnO where a small amount of ZnO to the coating increases the corrosion resistance. The resistance is due to the synergistic effect of the nanoparticles and the high surface area of the nano-sized ZnO particles increasing the barrier properties even after 30 days showing resistances higher than 108 Ωcm<sup>2</sup> [110].

It was also observed with TiO<sub>2</sub>- ZnO content in PVC coatings. The combination of these oxides increased the homogeneity of the coating, reducing the porosity blocking the corrosive ions into the polymeric coating of the film. With these two oxides and ZrO<sub>2</sub>, blocking and covering the coatings' defects increase the corrosion resistance. It has also been suggested that the metal ions of Zr<sup>+4</sup>/Ti<sup>+4</sup>/Zn<sup>+2</sup> encourage the reduction of oxygen vacancies reinforcing the resistance of the coatings [111]. The proposed transport and interfacial mechanisms are illustrated in Figure 21a-g. In Figure 21a, the physical interaction of the epoxy coating with the TMO nanoparticles and Figure 21b-j is the protection mechanism of the coatings against the aggressive environment showing the barrier.

Table 11 shows the corrosion resistance rate for different coatings and the metallic substrate at day 21. It can be observed the decrease of the *i*<sub>corr</sub> with the increase of the TiO<sub>2</sub> and

ZnO and the decrease of ZrO<sub>2</sub> content of the TMO. It is observed that the increase of the  $v_{corr}$  of the epoxy-A consistent with the results obtained in EIS. Coating epoxy-D is the one with the lowest corrosion rate of  $2.56 \times 10^{-7}$  mpy.



**Figure 21.** Corrosion protection mechanism of the epoxy coatings, a) physical interaction of the nanoparticles with the epoxy polymer, b) day 1, c) day 7, d) day 14, e) day 21, f) day 28

**Table 11.** Linear polarization resistance (LPR) of the coatings at 21 days

Sample	$E_{corr}$ ( $10^{-3}$ V)	$R_p$ ( $10^6 \Omega$ )	$i_{corr}$ ( $10^{-10}$ A/cm <sup>2</sup> )	$v_{corr}$ ( $10^{-7}$ mpy)
SS	-232.2	0.019	13032.58	16300
Epoxy	218.6	4.768	61.65	77.1
Epoxy-A	608.1	0.297	876.01	1095
Epoxy-B	124.8	63.09	4.12	5.15
Epoxy-C	22.39	66.10	3.93	4.91
Epoxy-D	45.55	126.9	2.05	2.56
Epoxy- E	41.82	53.79	4.83	6.04

## CHAPTER IV

### CONCLUSIONS

#### IV.1 Magnesium-rich coatings

The cathodic protection period depends on the magnesium content.

The addition of CNTs, enhances the connectivity when the concentration of Mg particles is low.

The addition of CNT's at higher concentrations of Mg particles, improves the conductivity of the coating and activates the magnesium particles in a shorter period.

#### IV.2 Trimetallic Oxides

The different characterizations showed that these epoxy-TMO coatings present different properties of UV absorbance, hydrophilic and barrier properties due to the combination and synergy of these three oxides. Epoxy- D coating with a TMO content of 50/40/10 (ZrO<sub>2</sub>/TiO<sub>2</sub>/ZnO) was the one to stand out. This composite coating not only presented higher hydrophilic properties compared to the other coatings, but also showed higher barrier properties by having resistance in the order of  $\sim 10^{12} \Omega\text{cm}^2$ .

## REFERENCES

1. Azeez, A.A., et al., *Epoxy clay nanocomposites – processing, properties and applications: A review*. Composites Part B: Engineering, 2013. **45**(1): p. 308-320.
2. Kandare, E., B.K. Kandola, and P. Myler, *Evaluating the influence of varied fire-retardant surface coatings on post-heat flexural properties of glass/epoxy composites*. Fire Safety Journal, 2013. **58**: p. 112-120.
3. Al-Turaif, H.A., *Relationship between tensile properties and film formation kinetics of epoxy resin reinforced with nanofibrillated cellulose*. Progress in Organic Coatings, 2013. **76**(2): p. 477-481.
4. Mohammed, I.A., M.F. Ali, and W.R. Wan Daud, *New class of liquid crystalline epoxy resins: Synthesis and properties*. Journal of Industrial and Engineering Chemistry, 2012. **18**(1): p. 364-372.
5. May, C., *Epoxy Resins: Chemistry and Technology, Second Edition*. 2018: CRC Press.
6. Craver, C.D., et al., *Applied Polymer Science : 21st Century*. 2000, Oxford, UNITED KINGDOM: Elsevier Science & Technology.
7. Chawla, S.L. and R.K. Gupta, *Materials Selection for Corrosion Control*. 1993.
8. Kissell, J.R. and R.L. Ferry, *Aluminum structures : a guide to their specifications and design. 2nd ed. J. Randolph Kissell, Robert L. Ferry*. 2002: New York : J. Wiley, [2002] 2nd ed.
9. DeRose, J.A., et al., *Aluminium Alloy Corrosion of Aircraft Structures : Modelling and Simulation*. 2012, Southampton, UNITED KINGDOM: WIT Press.
10. Gao, M., C.R. Feng, and R.P. Wei, *An analytical electron microscopy study of constituent particles in commercial 7075-T6 and 2024-T3 alloys*. Metallurgical and Materials Transactions A, 1998. **29**(4): p. 1145-1151.
11. Lee, W.-S., et al., *The strain rate and temperature dependence of the dynamic impact properties of 7075 aluminum alloy*. Journal of Materials Processing Technology, 2000. **100**(1): p. 116-122.
12. Kalkanli, A. and S. Yilmaz, *Synthesis and characterization of aluminum alloy 7075 reinforced with silicon carbide particulates*. Materials & Design, 2008. **29**(4): p. 775-780.
13. Ghali, E., *Aluminum and Aluminum Alloys*, in *Uhlig's Corrosion Handbook*. 2011. p. 715-745.
14. Committee, A.S.M.H., *Properties and Selection: Nonferrous Alloys and Special-Purpose Materials*. 1990, ASM International.
15. Scully, J.R., *Corrosion, Electrochemical Principles of*, in *Encyclopedia of Materials: Science and Technology*, K.H.J. Buschow, et al., Editors. 2001, Elsevier: Oxford. p. 1681-1686.
16. Perez, N., *Electrochemistry and corrosion science. by Nestor Perez*. 2004: Kluwer Academic Publishers.
17. Stansbury, E.E. and R.A. Buchanan, *Fundamentals of electrochemical corrosion. E.E. Stansbury and R.A. Buchanan*. 2000: ASM International.
18. Schmutz, P. and G.S. Frankel, *Influence of Dichromate Ions on Corrosion of Pure Aluminum and AA2024-T3 in NaCl Solution Studied by AFM Scratching*. Journal of The Electrochemical Society, 1999. **146**(12): p. 4461-4472.

19. Reboul, M.C. and B. Baroux, *Metallurgical aspects of corrosion resistance of aluminium alloys*. *Materials and Corrosion*, 2011. **62**(3): p. 215-233.
20. Pathak, S.S., et al., *Magnesium-Based Sacrificial Anode Cathodic Protection Coatings (Mg-Rich Primers) for Aluminum Alloys*. *Metals* (2075-4701), 2012. **2**(3): p. 353-376.
21. Munson, C.A. and G.M. Swain, *Structure and chemical composition of different variants of a commercial trivalent chromium process (TCP) coating on aluminum alloy 7075-T6*. *Surface and Coatings Technology*, 2017. **315**: p. 150-162.
22. Twite, R.L. and G.P. Bierwagen, *Review of alternatives to chromate for corrosion protection of aluminum aerospace alloys*. *Progress in Organic Coatings*, 1998. **33**(2): p. 91-100.
23. Guan, H. and R.G. Buchheit, *Corrosion Protection of Aluminum Alloy 2024-T3 by Vanadate Conversion Coatings*. *Corrosion*, 2004. **60**(3): p. 284-296.
24. Lin, J., et al., *(Mg rich primer-powder topcoat) coating system for the corrosion protection of Al alloys*. *Progress in Organic Coatings*, 2017. **102**: p. 138-143.
25. Nanna, M.E. and G.P. Bierwagen, *Mg-rich coatings: A new paradigm for Cr-free corrosion protection of Al aerospace alloys*. *JCT Research*, 2004. **1**(2): p. 69-80.
26. Xu, H., et al., *Use of Magnesium Alloys as Pigments in Magnesium-Rich Primers for Protecting Aluminum Alloys*. *Corrosion*, 2009. **65**(5): p. 318-325.
27. Bierwagen, G., et al., *Active metal-based corrosion protective coating systems for aircraft requiring no-chromate pretreatment*. *Progress in Organic Coatings*, 2010. **67**(2): p. 195-208.
28. Wang, Y.-P., et al., *Corrosion Protection of Ceria Particles in Mg-Rich Primer on AZ91D Magnesium Alloy*. *Acta Physico-Chimica Sinica*, 2012. **28**(2): p. 407-413.
29. Lu, X., et al., *The improved performance of a Mg-rich epoxy coating on AZ91D magnesium alloy by silane pretreatment*. *Corrosion Science*, 2012. **60**: p. 165-172.
30. Brown, R. *Protecting metal with magnesium*. 2007 [cited 2021 February 25, 2021].
31. Abdolahi, A., et al., *Application of Environmentally-Friendly Coatings Toward Inhibiting the Microbially Influenced Corrosion (MIC) of Steel: A Review*. *Polymer Reviews*, 2014. **54**(4): p. 702-745.
32. Fedel, M., et al., *Characterization of Polyorganosilazane-Derived Hybrid Coatings for the Corrosion Protection of Mild Steel in Chloride Solution*. *Coatings*, 2019. **9**(10).
33. Abreu, C.M., et al., *A New Approach to the Determination of the Cathodic Protection Period in Zinc-Rich Paints*. *Corrosion*, 1999. **55**(12): p. 1173-1181.
34. Tambe, S.P., et al., *Evaluation of microbial corrosion of epoxy coating by using sulphate reducing bacteria*. *Progress in Organic Coatings*, 2016. **94**: p. 49-55.
35. Cubides, Y. and H. Castaneda, *Corrosion protection mechanisms of carbon nanotube and zinc-rich epoxy primers on carbon steel in simulated concrete pore solutions in the presence of chloride ions*. *Corrosion Science*, 2016. **109**: p. 145-161.
36. Cubides, Y., S.S. Su, and H. Castaneda, *Influence of Zinc Content and Chloride Concentration on the Corrosion Protection Performance of Zinc-Rich Epoxy Coatings Containing Carbon Nanotubes on Carbon Steel in Simulated Concrete Pore Environments*. *Corrosion*, 2016. **72**(11): p. 1397-1423.
37. Park, S. and M. Shon, *Effects of multi-walled carbon nano tubes on corrosion protection of zinc rich epoxy resin coating*. *Journal of Industrial and Engineering Chemistry*, 2015. **21**: p. 1258-1264.



38. Pathak, S.S., et al., *Investigation on dual corrosion performance of magnesium-rich primer for aluminum alloys under salt spray test (ASTM B117) and natural exposure*. Corrosion Science, 2010. **52**(4): p. 1453-1463.
39. Strekalov, P.V., *The atmospheric corrosion of metals by adsorbed polymolecular moisture layers*. Protection of Metals, 1998. **34**: p. 501-519.
40. Martell, A.E. and R.M. Smith, *Critical stability constants*. by Arthur E. Martell and Robert M. Smith. 1974: Plenum Press.
41. Jönsson, M., D. Persson, and D. Thierry, *Corrosion product formation during NaCl induced atmospheric corrosion of magnesium alloy AZ91D*. Corrosion Science, 2007. **49**(3): p. 1540-1558.
42. White, W.B., *Thermodynamic equilibrium, kinetics, activation barriers, and reaction mechanisms for chemical reactions in Karst Terrains*. Environmental Geology, 1997. **30**(1): p. 46-58.
43. Duan, Z. and R. Sun, *An improved model calculating CO<sub>2</sub> solubility in pure water and aqueous NaCl solutions from 273 to 533 K and from 0 to 2000 bar*. Chemical Geology, 2003. **193**(3): p. 257-271.
44. Yao, H.B., Y. Li, and A.T.S. Wee, *An XPS investigation of the oxidation/corrosion of melt-spun Mg*. Applied Surface Science, 2000. **158**(1): p. 112-119.
45. Akbarinezhad, E., et al., *Another approach for ranking and evaluating organic paint coatings via electrochemical impedance spectroscopy*. Corrosion Science, 2009. **51**(2): p. 356-363.
46. Mansfeld, F., et al., *Evaluation of corrosion protection by polymer coatings using electrochemical impedance spectroscopy and noise analysis*. Electrochimica Acta, 1998. **43**(19): p. 2933-2945.
47. Mansfeld, F., *Use of electrochemical impedance spectroscopy for the study of corrosion protection by polymer coatings*. Journal of Applied Electrochemistry, 1995. **25**(3): p. 187-202.
48. Hu, J.M., J.Q. Zhang, and C.N. Cao, *Determination of water uptake and diffusion of Cl<sup>-</sup> ion in epoxy primer on aluminum alloys in NaCl solution by electrochemical impedance spectroscopy*. Progress in Organic Coatings, 2003. **46**(4): p. 273-279.
49. Leidheiser, H., *Electrical and electrochemical measurements as predictors of corrosion at the metal—organic coating interface*. Progress in Organic Coatings, 1979. **7**(1): p. 79-104.
50. Bierwagen, G., et al., *EIS studies of coated metals in accelerated exposure*. Progress in Organic Coatings, 2003. **46**(2): p. 149-158.
51. Kittel, J., et al., *Influence of the coating—substrate interactions on the corrosion protection: characterisation by impedance spectroscopy of the inner and outer parts of a coating*. Progress in Organic Coatings, 2003. **46**(2): p. 135-147.
52. Aperam. *What is Stainless Steel*. 2021 [cited 2021 March 20, 2021].
53. Shen, G.X., Y.C. Chen, and C.J. Lin, *Corrosion protection of 316 L stainless steel by a TiO<sub>2</sub> nanoparticle coating prepared by sol–gel method*. Thin Solid Films, 2005. **489**(1): p. 130-136.
54. Wang, D. and G.P. Bierwagen, *Sol–gel coatings on metals for corrosion protection*. Progress in Organic Coatings, 2009. **64**(4): p. 327-338.
55. Atik, M., et al., *Sol-gel thin films for corrosion protection*. Ceramics International, 1995. **21**(6): p. 403-406.

56. Husain, E., et al., *Marine Corrosion Protective Coatings of Hexagonal Boron Nitride Thin Films on Stainless Steel*. ACS Applied Materials & Interfaces, 2013. **5**(10): p. 4129-4135.
57. Liu, C.L., et al., *Anti-corrosion characteristics of nitride-coated AISI 316L stainless steel coronary stents*. Surface and Coatings Technology, 2006. **201**(6): p. 2802-2806.
58. Sathiyarayanan, S., et al., *Corrosion protection of steel by polyaniline (PANI) pigmented paint coating*. Progress in Organic Coatings, 2005. **53**(4): p. 297-301.
59. Behzadnasab, M., et al., *Corrosion performance of epoxy coatings containing silane treated ZrO<sub>2</sub> nanoparticles on mild steel in 3.5% NaCl solution*. Corrosion Science, 2011. **53**(1): p. 89-98.
60. Wessling, B. and J. Posdorfer, *Corrosion prevention with an organic metal (polyaniline): corrosion test results*. Electrochimica Acta, 1999. **44**(12): p. 2139-2147.
61. Ćurković, L., et al., *Enhancement of corrosion protection of AISI 304 stainless steel by nanostructured sol-gel TiO<sub>2</sub> films*. Corrosion Science, 2013. **77**: p. 176-184.
62. Shanaghi, A., et al., *Corrosion protection of mild steel by applying TiO<sub>2</sub> nanoparticle coating via sol-gel method*. Protection of Metals and Physical Chemistry of Surfaces, 2009. **45**(3): p. 305-311.
63. Chung, C.-J., et al., *Multifunctional arc ion plated TiO<sub>2</sub> photocatalytic coatings with improved wear and corrosion protection*. Surface and Coatings Technology, 2009. **203**(12): p. 1689-1693.
64. Kamachimudali, U., T.M. Sridhar, and B. Raj, *Corrosion of bio implants*. Sadhana, 2003. **28**(3): p. 601-637.
65. Yaghoubi, H., et al., *Nanomechanical Properties of TiO<sub>2</sub> Granular Thin Films*. ACS Applied Materials & Interfaces, 2010. **2**(9): p. 2629-2636.
66. Maier, B. and G.S. Frankel, *Behavior of Magnesium-Rich Primers on AA2024-T3*. CORROSION, 2011. **67**(5): p. 055001-1-055001-15.
67. Kannan, B., et al., *Performance of a Magnesium-Rich Primer on Pretreated AA2024-T351 in Full Immersion: a Galvanic Throwing Power Investigation Using a Scanning Vibrating Electrode Technique*. Journal of The Electrochemical Society, 2018. **165**(2): p. C27-C41.
68. Michael, D.B., et al., *Magnesium-Based Sacrificial Anode Cathodic Protection Coatings (Mg-Rich Primers) for Aluminum Alloys*. Metals, 2012(3): p. 353.
69. Lu, X., et al., *The study of a Mg-rich epoxy primer for protection of AZ91D magnesium alloy*. Corrosion Science, 2011. **53**(1): p. 153-160.
70. Battocchi, D., et al., *Electrochemical behaviour of a Mg-rich primer in the protection of Al alloys*. Corrosion Science, 2006. **48**(5): p. 1292-1306.
71. Allahar, K.N., et al. *Transmission Line Modeling of EIS Data for a Mg-Rich Primer on AA 2024-T3*. 2008. Pennington, N.J.; Electrochemical Society.
72. Lin, J., D. Battocchi, and G.P. Bierwagen, *Degradation of magnesium-rich primers over AA2024-T3 during constant immersion in different solutions*. Corrosion, 2017. **73**(4): p. 408-416.
73. King, A.D. and J.R. Scully, *Sacrificial Anode-Based Galvanic and Barrier Corrosion Protection of 2024-T351 by a Mg-Rich Primer and Development of Test Methods for Remaining Life Assessment*. 2011.
74. Bierwagen, G.P., *Reflections on corrosion control by organic coatings*. Progress in Organic Coatings, 1996. **28**(1): p. 43-48.

75. Lu, X., et al., *The effects of magnesium particles in Mg-rich primers applied on AZ91D magnesium alloy*. 2015. **10**: p. 9586-9604.
76. Mathiazhagan, A. and R. Joseph, *Nanotechnology-A New Prospective in Organic Coating -Review*. Vol. 2. 2011. 225-237.
77. Turhan, M.C., et al., *Corrosion behaviour of multiwall carbon nanotube/magnesium composites in 3.5% NaCl*. *Electrochimica Acta*, 2011. **56**(20): p. 7141-7148.
78. Liu, J., et al., *Promoting Barrier Performance and Cathodic Protection of Zinc-Rich Epoxy Primer via Single-Layer Graphene*. *Polymers (Basel)*, 2018. **10**(6).
79. Cai, Y., et al., *Anticorrosion and Scale Behaviors of Nanostructured ZrO<sub>2</sub>-TiO<sub>2</sub> Coatings in Simulated Geothermal Water*. *Industrial & Engineering Chemistry Research*, 2016. **55**(44): p. 11480-11494.
80. Heidarian, M., et al., *Characterization of structure and corrosion resistivity of polyurethane/organoclay nanocomposite coatings prepared through an ultrasonication assisted process*. *Progress in Organic Coatings*, 2010. **68**(3): p. 180-188.
81. Ibrahim, M., et al., *Enhanced Corrosion Protection of Epoxy/ZnO-NiO Nanocomposite Coatings on Steel*. *Coatings*, 2020. **10**(8).
82. Dastgheib, A., A. Zarebidaki, and M.M. Attar, *Enhanced barrier properties of epoxy coating containing CaCO<sub>3</sub> microparticles modified with cerium nitrate*. *Progress in Organic Coatings*, 2020. **144**: p. 105660.
83. González-García, Y., S. González, and R.M. Souto, *Electrochemical and structural properties of a polyurethane coating on steel substrates for corrosion protection*. *Corrosion Science*, 2007. **49**(9): p. 3514-3526.
84. Pirhady Tavandashti, N., S. Molana Almas, and E. Esmaeilzadeh, *Corrosion protection performance of epoxy coating containing alumina/PANI nanoparticles doped with cerium nitrate inhibitor on Al-2024 substrates*. *Progress in Organic Coatings*, 2021. **152**: p. 106133.
85. Aslam, J., et al., *Corrosion protection of low carbon steel by conducting terpolymer nanocomposite coating in 3.5 wt% NaCl solution*. *Journal of Adhesion Science and Technology*, 2020. **34**(4): p. 443-460.
86. Al-Daraghme, M.Y., M.T. Hayajneh, and M.A. Almomani, *Corrosion Resistance of TiO<sub>2</sub>-ZrO<sub>2</sub> Nanocomposite Thin Films Spin Coated on AISI 304 Stainless Steel in 3.5 wt. % NaCl Solution*. *Materials Research*, 2019. **22**.
87. Precious Ayanwale, A. and S.Y. Reyes-López, *ZrO<sub>2</sub>-ZnO Nanoparticles as Antibacterial Agents*. *ACS Omega*, 2019. **4**(21): p. 19216-19224.
88. Bavykin, D.V., et al., *The effect of hydrothermal conditions on the mesoporous structure of TiO<sub>2</sub> nanotubes*. *Journal of Materials Chemistry*, 2004. **14**(22): p. 3370-3377.
89. Deyab, M.A., A.A. Nada, and A. Hamdy, *Comparative study on the corrosion and mechanical properties of nano-composite coatings incorporated with TiO<sub>2</sub> nanoparticles, TiO<sub>2</sub> nano-tubes, and ZnO nano-flowers*. *Progress in Organic Coatings*, 2017. **105**: p. 245-251.
90. Zhuang, J., et al., *Construction of novel ZnTiO<sub>3</sub>/g-C<sub>3</sub>N<sub>4</sub> heterostructures with enhanced visible light photocatalytic activity for dye wastewater treatment*. *Journal of Materials Science: Materials in Electronics*, 2019. **30**.
91. Štefanić, G., S. Musić, and M. Ivanda, *Phase development of the ZrO<sub>2</sub>-ZnO system during the thermal treatments of amorphous precursors*. *Journal of Molecular Structure*, 2009. **924-926**: p. 225-234.

92. Uribe López, M.C., et al., *Synthesis and Characterization of ZnO-ZrO<sub>2</sub> Nanocomposites for Photocatalytic Degradation and Mineralization of Phenol*. Journal of Nanomaterials, 2019. **2019**: p. 1015876.
93. Simon, S.M., et al., *Development of Thick Superhydrophilic TiO<sub>2</sub>-ZrO<sub>2</sub> Transparent Coatings Realized through the Inclusion of Poly(methyl methacrylate) and Pluronic-F127*. ACS Omega, 2018. **3**(11): p. 14924-14932.
94. deBakker, C.J., et al., *The kinetics of the cure of an advanced epoxy resin by Fourier transform Raman and near-IR spectroscopy*. Spectrochimica Acta Part A: Molecular Spectroscopy, 1993. **49**(5): p. 739-752.
95. Nikafshar, S., et al., *The Effects of UV Light on the Chemical and Mechanical Properties of a Transparent Epoxy-Diamine System in the Presence of an Organic UV Absorber*. Materials (Basel), 2017. **10**(2).
96. Xu, H., et al., *Preparation of porous TiO<sub>2</sub>/ZnO composite film and its photocathodic protection properties for 304 stainless steel*. Applied Surface Science, 2014. **301**: p. 508-514.
97. Horti, N.C., et al., *Structural and optical properties of zirconium oxide (ZrO<sub>2</sub>) nanoparticles: effect of calcination temperature*. Nano Express, 2020. **1**(1): p. 010022.
98. Sathyaseelan, B., et al., *Studies on structural and optical properties of ZrO<sub>2</sub> nanopowder for opto-electronic applications*. Journal of Alloys and Compounds, 2017. **694**: p. 556-559.
99. Xie, Y., Y. Jiang, and S. Zhao, *Improving the wettability on ZnO and ZrO<sub>2</sub> single crystal surface by laser irradiation*. International Congress on Applications of Lasers & Electro-Optics, 2012. **2012**(1): p. 943-946.
100. Nikoomanzari, E., et al., *Effect of ZrO<sub>2</sub> nanoparticles addition to PEO coatings on Ti-6Al-4V substrate: Microstructural analysis, corrosion behavior and antibacterial effect of coatings in Hank's physiological solution*. Ceramics International, 2020. **46**(9): p. 13114-13124.
101. Banerjee, S., D.D. Dionysiou, and S.C. Pillai, *Self-cleaning applications of TiO<sub>2</sub> by photo-induced hydrophilicity and photocatalysis*. Applied Catalysis B: Environmental, 2015. **176-177**: p. 396-428.
102. Sanu, M.S., et al., *Synthesis and hydrophilic mechanism of porous TiO<sub>2</sub>-ZrO<sub>2</sub> transparent coatings*. AIP Conference Proceedings, 2019. **2082**(1): p. 030031.
103. Ferrel-Alvarez, A.C., et al., *Intensification of Electrochemical Performance of AA7075 Aluminum Alloys Using Rare Earth Functionalized Water-Based Polymer Coatings*. Polymers (Basel), 2017. **9**(5).
104. El-Mahdy, G.A., A.M. Atta, and H.A. Al-Lohedan, *Synthesis and characterizations of Fe<sub>3</sub>O<sub>4</sub> nanogel composite for enhancement of the corrosion resistance of steel in HCl solutions*. Journal of the Taiwan Institute of Chemical Engineers, 2014. **45**(4): p. 1947-1953.
105. Miramontes, J.A., *Corrosion behavior of Zn-TiO<sub>2</sub> and Zn-ZnO Electrodeposited Coatings in 3.5% NaCl solution*. International Journal of Electrochemical Science, 2019. **14**: p. 4226-4239.
106. Shafaamri, A., et al., *Effects of TiO<sub>2</sub> Nanoparticles on the Overall Performance and Corrosion Protection Ability of Neat Epoxy and PDMS Modified Epoxy Coating Systems*. Frontiers in Materials, 2020. **6**.

107. Kumar, K., P.K. Ghosh, and A. Kumar, *Improving mechanical and thermal properties of TiO<sub>2</sub>-epoxy nanocomposite*. Composites Part B: Engineering, 2016. **97**: p. 353-360.
108. Ramezanzadeh, B. and M.M. Attar, *Studying the effects of micro and nano sized ZnO particles on the corrosion resistance and deterioration behavior of an epoxy-polyamide coating on hot-dip galvanized steel*. Progress in Organic Coatings, 2011. **71**(3): p. 314-328.
109. Khosravi H, S., et al., *Effect of processing conditions on the structural properties and corrosion behavior of TiO<sub>2</sub>-SiO<sub>2</sub> multilayer coatings derived via the sol-gel method*. Ceramics International, 2020. **46**(11, Part A): p. 17741-17751.
110. Abdus Samad, U., et al., *Effect of Incorporated ZnO Nanoparticles on the Corrosion Performance of SiO<sub>2</sub> Nanoparticle-Based Mechanically Robust Epoxy Coatings*. Materials (Basel), 2020. **13**(17).
111. Abd El-Lateef, H.M., A.O. Alnajjar, and M.M. Khalaf, *Advanced self-healing coatings based on ZnO, TiO<sub>2</sub>, and ZnO-TiO<sub>2</sub>/polyvinyl chloride nanocomposite systems for corrosion protection of carbon steel in acidic solutions containing chloride*. Journal of the Taiwan Institute of Chemical Engineers, 2020. **116**: p. 286-302.